Towards the Real-Time Control of Divertor Target Conditions in the TCV Using Kalman Filters and SOLPS-ITER to Observe the Divertor Region

Savona, Isaac A.

Award date:
2024

EINDHOVEN UNIVERSITY OF TECHNOLOGY

Department of Applied Physics and Science Education

Towards the Real-Time Control of Divertor Target Conditions in the TCV: Using Kalman Filters and SOLPS-ITER to Observe the Divertor Region

by

I.A.S. Savona

MSC THESIS

Assessment committee

Member 1 (chair):	Prof.dr., M.R., de Baar
Member 2:	Prof.dr., R.J.E., Jaspers
Member 3:	Dr.ir., K.H.A., Verhaegh

Graduation

Program:	Science and Technology of Nuclear Fusion
Capacity group:	Energy Systems and Control
Supervisor:	Prof.dr., R.J.E., Jaspers
Date of defense:	September 23, 2024
Student ID:	1828886
Study load (ECTS):	60

The research of this thesis has been carried out in collaboration with *the Dutch Institute for Fundamental Energy Research*.

Abstract

The effect of injecting impurity gasses has been a key tool for fusion researchers in mitigating high heat fluxes on tokamak divertor targets. Yet research has thus far not been able to yield control-oriented models of the divertor region which enable predictions on the condition of the divertor target. Such a model would allow for a controller to inject impurity gasses based on predicted divertor target conditions and, therefore, have the chance to mitigate potential target failures. In this thesis, the application of two different divertor models, partially derived from 55 SOLPS-ITER simulations, in combination with a Kalman Filter are shown to correlate strongly with the perpendicular heat flux on the outer target of the Tokamak à Configuration Variable (TCV) during L-mode discharges. Using steady-state information from static SOLPS-ITER simulations of the TCV covering a wide range of gas injection scenarios in L-mode, two linear time-invariant models were made to each model the dynamic evolution of two physical parameters – area-averaged nitrogen density n_N and neutral pressure p_0 – with respect to the injection of D_2 and N_2 gas. Kalman Filters were tuned to reconstruct these two parameters based on signals from the Multispectral Advanced Narrowband Tokamak Imaging System (MANTIS). The same SOLPS-ITER simulations were then used to create correlations between n_N and p_0 and the maximum electron temperature, perpendicular ion flux, and perpendicular heat flux on the divertor ($q_?^{tar;max}$) target. Six control-oriented, L-mode experiments on the TCV were analyzed using these models. For one of these models, the average RMSE over the six experiments, with respect to predicting $q_?^{tar;max}$, was approximately 42,280 W with a standard deviation of 3,661 W. With further analysis of different L-mode control-relevant experiments this thesis could be used in the real-time control of the outer divertor target conditions on the TCV. Future work could also prove the methods presented here useful in mitigating the water-cooled tungsten-target $q_?^{tar;max}$ limit of 10MWm ^{2} [18] which is expected for fusion reactors such as ITER.

Preface

> The craftsman of the Middle Ages no doubt often suffered grievous material oppression, yet in spite of the rigid line of separation drawn by the hierarchical system under which he lived between him and his feudal superior, the difference between them was arbitrary rather than real
>
> *William Morris*

Academic research is really a battle against one's own patience powered by a frustratingly endless curiosity to find those things which are not yet known and append it to an ever-growing framework of human understanding. I do not believe this framework will ever be able to truly describe reality, but it is nonetheless a fun process expanding it in ways that it may be of some use to humanity.

I couldn't have made this contribution to this framework without help from real people. First and foremost, I'd like to thank my girlfriend Charlotte Buijtelaar for always supporting me and encouraging me throughout this whole process of coming to the Netherlands and pursuing a master's degree. Additionally, I'd like to thank my family back in the states for enabling me to continue to learn about the world inside and outside of the classroom. Moving on to the academic side of things, I'd first like to thank Jorn Veenendaal for helping me out on the day to day and allowing me to pester him with questions. In a similar vein I'd like to thank the TCV team for answering questions via email about sensors, matlab functions and SOLPS-ITER. A big thanks also goes to Gijs Derks for helping me acquire data in the early days of my research when I could not get access to the servers for technical. Finally, a thank you to Marco de Baar and Matthijs van Berkel for giving me the opportunity to contribute to this line of research. I hope I gave a good first step.

Contents

Contents vii

List of Figures ix

List of Tables xi

1 Introduction 1
1.1 Nuclear Fusion . . . 1
1.2 The Tokamak . . . 2
1.3 The Divertor: The Tokamak's Exhaust . . . 3
1.4 Loss Mechanisms and Detachment . . . 4
1.5 Divertor Control . . . 4
1.6 Research Question . . . 5
1.7 Outline . . . 5

2 Background 7
2.1 SOLPS-ITER . . . 7
2.2 State-Space and Observer . . . 7
2.3 Le Tokamak a Con guration Variable . . . 9
2.3.1 The TCV's Loss Mechanisms . . . 9
2.4 Gas Valves . . . 10
2.5 A Note On Measurement Rate . . . 10
2.6 Bolometers . . . 11
2.7 MANTIS and y_{NII} . . . 12
2.8 FIR . . . 13
2.9 VIR . . . 13

3 Methods 15
3.1 Motivating the Choice of State . . . 15
3.2 Experiments Used . . . 16
3.3 SOLPS-ITER Simulations Used . . . 16
3.4 Leveraging SOLPS-ITER for a Dynamic Model . . . 17
3.4.1 Steady-State Condition and State-Space Model . . . 17
3.4.2 Relationship to Diagnostics . . . 20
3.5 Using a Transformed Di usion Model . . . 21
3.6 Kalman lters . . . 23
3.6.1 Integration Model . . . 23
3.6.2 Koenders' Transformed Model . . . 24
3.7 Validation . . . 25

4 Results 27
4.1 Steady-State Fits and the Integration Model 27
4.2 Synthetic Diagnostic Fits 28
4.3 Target Quantity Fits 29
4.4 Kalman lter with Integration Model 31
4.4.1 Kalman lter: Input, Output, and State 32
4.4.2 Validation of KF Performance 37
4.5 Koenders' Transformed Model 40
4.6 KF with Koenders' Transformed Model 40
4.6.1 Kalman lter: Input, Output, and State 41
4.6.2 Validation of KF Performance 44

5 Conclusions 47
5.1 Discussion 47
5.1.1 Methods 47
5.1.2 Results 48
5.2 Outlook 49
5.2.1 Dynamic Model Improvements 49

Bibliography 51

Appendix 55

Appendix 55

Appendix 55

A Extra Shots 55
A.1 Kalman Filter with Integration Model 55
A.2 KF with Koenders' Transformed Model 63

B Using the Bolometers 72
B.1 Data Complications 72
B.2 Synthetic Diagnostic 72
B.3 Other Errata Found 72

C Identi cation Strategy 73

List of Figures

1.1 Schematic [31] of deuterium (one proton and one neutron) and tritium (two neutrons and one proton) nuclei fusing with output energies labeled. 2
1.2 A simpli ed schematic of a tokamak from EUROFusion showing the magnets, as well as the resulting magnetic eld line geometry needed to contain the plasma. Notice how the helical magnetic eld line, the result of the toroidal and poloidal magnetic eld, spirals around the torus both toroidally and poloidally. 2
1.3 Simple depiction of nested toroidal ux surfaces. This poloidal representation is relevant to understanding the model used in this thesis. 3
1.4 A simple schematic of a tokamak's core, SOL, and divertor targets from [17]. The particles make their way out of the core and down to the divertor plates (i.e., the targets). The separatrix is the name for the LCFS in the diverted con guration. . 4
1.5 An example of the neutral pressure during an L-mode discharge in the TCV as simulated by SOLPS-ITER 5

2.1 Cross-section of TCV showing the central solenoid, poloidal eld coils, and toroidal eld coils. Image by M. Toussaint 9
2.2 A schematic of a gold-foil bolometer sensor 11
2.3 The complete RADCAM system including two sensors which are not discussed here, SXR and AXUV. More information can be found in [22]. 11
2.5 Poloidal schematic showing the vantage point of the VIR from the EPFL wiki . . . 13

3.1 A grid of the 55 SOLPS-ITER simulations used in this thesis of the two parameters n_N and p_0. This can be used as a reference for how these parameters vary spatially across di erent SOLPS-ITER simulations. 18
3.2 The regions in SOLPS-ITER over which the states n_N and p_0 are averaged. This is an example from SOLPS-ITER simulation with MDS number 127719 20
3.3 Two linearly-regressed ts which describe the steady-state relationship between the gas pu s u and the state x over the 55 SOLPS-ITER simulations. Notice the 55 red dots in each plot. 21
3.4 KF algorithm 24

4.1 Two linearly-regressed ts which describe the steady-state relationship between the gas pu s u and the state x over the 55 SOLPS-ITER simulations. Notice the 55 red dots in each plot. 28
4.2 Two linearly regressed ts based on a synthetic diagnostic [14] of MANTIS in SOLPS-ITER which takes into account the emission from di erent ions in SOLPS-ITER from the ADAS database [1]. 29
4.3 The least-squares tted function relating the state parameters to critical target quantities over the 55 simulations. Here, Wilkinson notation is used [15] and therefore $_1$ and $_2$ correspond to coe cients multiplied by n_N, p_0 and respectively. . . 30

4.4 The least-squares tted function relating the state parameters to critical target quantities over the 55 simulations. Here, Wilkinson notation is used [15] and therefore $_1$ and $_2$ correspond to coe cients multiplied by n_N, p_0 and respectively. . . 31
4.5 From top to bottom: the input, state, output and KF residual evolutions from shot #69148. In the state and output plots, both show the model acting on its own without measurement updates. 33
4.6 Input, state, KF and output evolution during shot #69148. 35
4.7 From top to bottom: the input, state, output and KF residual evolutions from shot #69145. In the state and output plots, both show the model acting on its own without measurement updates. 35
4.8 Step response for the 80 parameters. Because the A matrix is sparse, only the rst 40 states are actuated by N_2 and the last 40 states are actuated by D_2. The dark blue signals are barely visible because they decay so quickly. 41
4.9 From top to bottom: the input, state, output and KF residual evolutions from shot #69145. In the state and output plots, both show the model acting on its own without measurement updates. 42
4.10 From top to bottom: the input, state, output and KF residual evolutions from shot #69148. In the state and output plots, both show the model acting on its own without measurement updates. 43

A.1 Comparison of plots and residuals for case 68861. 56
A.2 58
A.3 60
A.4 62
A.5 64
A.6 66
A.7 68
A.8 70

List of Tables

2.1 Some operational parameter ranges of the TCV experiments from the EPFL wiki. De nitions of these geometric quantities can be found in external resources [8] . . . 10

3.1 The 55 SOLPS-ITER simulations used. Each simulation's MDS (fusion database) number corresponds with their respective in uxes of D_2 and N_2 in particles per second. A complete list of the loss mechanisms present in these simulations can be found in [25]. . . . 16

3.2 Comparing the averaged outer-midplane electron density on the separatrix across the SOLPS-ITER simulations and experiments #68861, #69147, #69144, #69185, #69145, and #69148. The experiments used Thomson Scattering measurements to obtain an estimate on $n_e^{sep;omp}$ . . . 17

4.1 Key for target analysis plots. Heref () is the analytic function that was presented in 3.24. RMSE(a,b) means the root mean square error between a and b. . . . 37

4.2 RMSE values for di erently regressed variables predicting $q_?^{tar;max}$. See 4.1 for a reference to what these variables mean. . . . 38

4.3 RMSE values for di erently regressed variables predicting $q_?^{tar;max}$. See 4.1 for a reference to what these variables mean. . . . 39

4.4 R-squared values for linearly transforming Koenders' di usion model to the desired SOLPS-ITER state parameters n_N and p_0. . . . 40

4.5 RMSE values for di erently regressed variables predicting $q_?^{tar;max}$. See 4.1 for a reference to what these variables mean. . . . 44

4.6 RMSE values for di erently regressed variables predicting $q_?^{tar;max}$. See 4.1 for a reference to what these variables mean. . . . 45

5.1 Mean RMSE values and standard deviations of the RMSEs for each variable across six experiments when using the Integration Model . . . 48

5.2 Mean RMSE values and standard deviations of the RMSEs for each variable across six experiments when using the Koenders' Transformed Model . . . 48

A.1 RMSE values for di erently regressed variables predicting $q_?^{tar;max}$ . . . 57

A.2 RMSE values for di erently regressed variables predicting $q_?^{tar;max}$ . . . 59

A.3 RMSE values for di erently regressed variables predicting $q_?^{tar;max}$ . . . 61

A.4 RMSE values for di erently regressed variables predicting $q_?^{tar;max}$ . . . 63

A.5 RMSE values for di erently regressed variables predicting $q_?^{tar;max}$ . . . 65

A.6 RMSE values for di erently regressed variables predicting $q_?^{tar;max}$ . . . 67

A.7 RMSE values for di erently regressed variables predicting $q_?^{tar;max}$ . . . 69

A.8 RMSE values for di erently regressed variables predicting $q_?^{tar;max}$ . . . 71

Chapter 1

Introduction

The contents of this thesis, like many theses, seek to o er a solution, or at least the beginning of one, to a particular problem. Additionally, as the problem in question is of an engineering nature, there is a speci c underlying motivation connected to a larger issue that a ects humanity climate change.

Climate change refers to the shifting patterns of weather historically observed across the planet. Without going into detail, research over the last few decades has shown that much of this change, and its negative consequences for life on Earth, is due to humans emitting greenhouse gases such as carbon dioxide and methane [10]. A large portion of human-induced greenhouse gas emissions not to mention other pollutants harmful to living organisms comes from electricity production using oil, coal, and natural gas [21]. Various cleaner (i.e., in reference to greenhouse gases being dirty) solutions have been proposed to address this issue, including nuclear ssion, solar, wind, and hydroelectric power. Each of these solutions has its own unique potential limitations when addressing climate change on its own [10], making it bene cial for humanity to broaden the portfolio of cleaner energy solutions.

A major bene t of this expanded clean energy portfolio would be the inclusion of an energy source that, like coal and natural gas, could increase or decrease electricity production as needed. This type of energy source is called a baseload energy source. Research is currently being conducted into cleaner baseload energy sources such as advanced geothermal [2][3], next-generation ssion plants [5] [4], and nuclear fusion. Nuclear fusion, as a potential energy source, promises to be clean, abundant, and safe by leveraging the fundamental process that powers the Sun. The aim of this series of introductory sections is to provide a broad overview of what nuclear fusion is, why magnetically con ning a high-power fusion plasma is so di cult (and what it means), what technical approaches have been implemented to address these challenges, and nally, how the methods presented in this thesis tackle a critical problem faced by current nuclear reactors. This will by no means be a comprehensive survey of the theory, engineering, and economics of nuclear fusion such information is treated in sources such as [10] [8]. Instead, this introduction will o er a su cient level of understanding for someone with a scienti c background to grasp and hopefully replicate the work carried out in this thesis.

1.1 Nuclear Fusion

Nuclear fusion is the process by which two nuclei overcome the Coulomb force repelling them, allowing the nuclear force to attract them together. Once fused, the mass of the combined product is smaller than the sum of the individual nuclei. This discrepancy in mass is expressed as a tremendous amount of energy. Under ideal conditions, using the hydrogen isotopes deuterium and tritium, it takes about 15 keV to have the highest chance of overcoming this barrier, whereas the fusion reaction releases about 17.6 MeV [10], as shown in 1.1.

To achieve these ideal conditions, where nuclei optimally produce fusion reactions, the nuclei

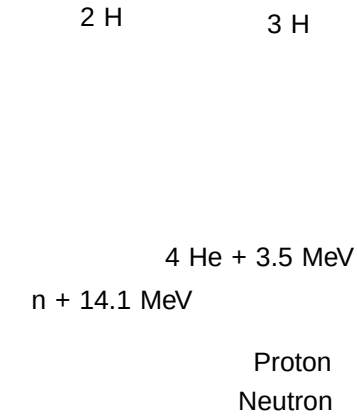

Figure 1.1: Schematic [31] of deuterium (one proton and one neutron) and tritium (two neutrons and one proton) nuclei fusing with output energies labeled.

must be kept at high temperatures and densities for a su ciently long period. In this way the particles have enough time existing closer to each other and in an energetic enough state where fusion is possible.

1.2 The Tokamak

A promising candidate device for creating these conditions is the tokamak. The name "tokamak" comes from a Russian acronym:

òî ðîèäàëüíàÿ êàìåðà ñ ìà ãíèòíûìè êàòóøêàìè
toroidal chamber with magnetic coils

Before explaining how the tokamak works to con ne particles, consider rst that in order to expose the nuclei (of hydrogen isotopes), the electrons must rst dissociate from the nuclei, leaving them free to collide with each other. In this state of free- owing ionized matter, known as plasma, charged particles can be guided by magnetic eld lines, an application of the Lorentz force. The tokamak uses magnetic eld lines that run both toroidally and poloidally around the torus 1.2 to keep the ionized particles con ned as the density and heat are increased to optimal fusion conditions.

Figure 1.2: A simpli ed schematic of a tokamak from EUROFusion showing the magnets, as well as the resulting magnetic eld line geometry needed to contain the plasma. Notice how the helical magnetic eld line, the result of the toroidal and poloidal magnetic eld, spirals around the torus both toroidally and poloidally.

This con guration of magnetic eld lines creates di erent magnetic helicities as a function of the distance from the center of the torus. These layers of di erent helicity are referred to as

surfaces since they run axisymmetrically around the torus. Because of this axisymmetry, poloidal cross-sections are often used to describe the entire torus.

Figure 1.3: Simple depiction of nested toroidal ux surfaces. This poloidal representation is relevant to understanding the model used in this thesis.

1.3 The Divertor: The Tokamak's Exhaust

Nested ux surfaces will eventually make contact with the reactor's wall. The closed, nested magnetic ux surfaces will then form connection points with the wall. The last closed ux surface is abbreviated as LCFS. This contact with the wall poses a problem, as the plasma can reach millions of degrees, and these magnetic eld lines create a direct path to the wall. When hydrogen ions impinge on the wall surface, two phenomena become signi cant: physical and chemical sputtering. Physical sputtering relates to the amount of kinetic energy with which hydrogen ions strike the wall, directly in uencing how much wall material is ejected from the surface. Chemical sputtering involves the chemical interactions between the hydrogen ions and the wall surface, which deteriorates the material. In both cases, heavy impurities enter the plasma, radiating power and decreasing the amount of fusion power that can be produced [27].

The "divertor" is the current engineering solution to this problem in tokamaks. By creating a magnetic null through inducing currents in the plasma that oppose the total plasma current, magnetic eld lines outside the LCFS are directed away from the main body of the plasma. This magnetic null is known as the x-point. The magnetic eld lines just outside the LCFS, which are diverted away from the plasma, form the Scrape-O Layer (SOL). As particles move radially outward, they follow the SOL down to speci c targets called divertor targets.

The divertor con guration helps to keep impurity production away from the core. Another bene t of the divertor region is that it locally creates a cooler area where ions can recombine into neutrals. As the neutral pressure increases, the e ciency of pumps improves, allowing for the exhaust of impurities such as spent fuel in the form of helium.

Additionally, future tokamaks like ITER and DEMO are expected to experience incredibly high heat loads on the divertor targets, exceeding the material limitations of the targets [18]. For water-cooled tungsten targets, this limit is around 10 MW/m 2 2 . The divertor thus serves as a region where impurity gases can be intentionally injected to cause the plasma to lose energy before it reaches the target. These loss mechanisms will be discussed in more detail, as understanding the e ects of injecting impurity gases into the divertor is essential for interpreting the results of this thesis.

Figure 1.4: A simple schematic of a tokamak's core, SOL, and divertor targets from [17]. The particles make their way out of the core and down to the divertor plates (i.e., the targets). The separatrix is the name for the LCFS in the diverted con guration.

1.4 Loss Mechanisms and Detachment

The term "detachment" refers to a regime characterized by lower target temperature and reduced particle ux, which is favorable for protecting the divertor targets from extreme conditions. One method to achieve detachment is by injecting impurity gases.

However, injecting too much impurity gas can lead to a rapid cooling of the plasma, resulting in an unstable condition known as radiative collapse. The plasma loses power primarily through volumetric recombination, line radiation, and plasma-neutral interactions. Volumetric recombination occurs when electrons are recaptured by ions in the plasma. This process reduces the energy of ions traveling towards the target and increases the neutral density. This phenomenon generally occurs when the temperature drops below approximately 1 eV [27], which typically happens in the divertor region. Therefore, power must be radiated in the SOL to enable volumetric recombination in the divertor.

Other power loss mechanisms are also at play, but the most signi cant in the SOL, for the purposes of this thesis, are related to the introduction of impurities (i.e., non-fuel species) into the plasma. These impurities primarily cause energy losses through line radiation, where ions or neutrals lose energy via radiation as their electrons transition between energy levels. Plasma-neutral interactions also contribute to energy losses in the divertor and SOL, particularly through charge-exchange interactions and ion-neutral collisions. Charge-exchange interactions occur when a neutral atom transfers its electron to an ion. If the neutral atom has lower energy than the ion, the ion becomes a fast neutral atom, while the neutral atom becomes a slower ion. Both processes result in momentum and energy losses from the SOL.

Additionally, when plasma interacts with the target, it can recombine with the wall material and then be re-ionized by incoming power, resulting in a continuous energy loss near the target.

With all these factors in mind, there clearly needs to be a correct amount of impurity introduced into the plasma, such that the divertor target is protected from damage without causing the plasma to radiatively collapse.

1.5 Divertor Control

Several attempts have been made to control the divertor, for example by using radiated power measurements in active feedback control [9]. However, these methods typically require tuning a gas valve controller over several plasma shots. In future reactors, there will be less time and fewer resources available to run multiple control shots to ne-tune such a controller. Furthermore,

radiative collapses could potentially be catastrophic for future reactors like ITER. This necessitates control-oriented models that can be tuned o ine. Recent research by Jesse Koenders [12] on Le Tokamak a Con guration Variable (the TCV) 2 has explored such control-oriented dynamic models. The model developed by Koenders is based on a di usion model and static data from one of the leading simulations used today for simulating the divertor region and SOL: the Scrape-O Layer Plasma Simulation for the International Thermonuclear Experimental Reactor (SOLPS-ITER). SOLPS-ITER uses Monte Carlo uid dynamics to provide 2-D spatially resolved plasma quantities.

This thesis research begins by exploring whether more can be leveraged from the dynamic model beyond just steady-state behavior. What if it were also possible to gain insight into other spatially resolved quantities in SOLPS-ITER, such as heat uxes, temperatures, ion uxes, impurity densities, etc.? In that case, one might be able to control the conditions at the target and avoid radiative collapse.

1.6 Research Question

This thesis seeks to answer the following question:Can an observer be designed to reconstruct SOLPS-ITER parameters based on real-time measurements of the TCV divertor, for the purposes of modeling the conditions at the divertor target? To clarify what an observer is, a more detailed explanation is provided in 2. In simple terms, an observer is an algorithm that uses a model to make predictions about a physical quantity and actively corrects those predictions based on real measurements. An observer reconstructs parameters by using measurements to adjust the model's parameters to better match the observed signal. Observers are not new to fusion research. A well-known example in the eld is RAPDENS, which is used to reconstruct the electron density pro le in the plasma core based on FIR measurements [7]. In this case, the reconstructed SOLPS-ITER parameters should be able to provide insights into the conditions at the divertor target.

Figure 1.5: An example of the neutral pressure during an L-mode discharge in the TCV as simulated by SOLPS-ITER

1.7 Outline

Now that a brief overview and motivation for the research presented in this thesis have been provided, the thesis will proceed with a more detailed background on the relevant theories. This will include an explanation of how SOLPS-ITER works and the motivation for using it. Following this, an introduction to the discrete-time, state-space formulation will be provided, along with a detailed explanation of how linear, discrete-time Kalman lters work to optimally estimate the state. This background will also include an overview of the TCV and its relevant sensors. Afterward, the use of these theories to develop an observer for the TCV will be explained and motivated. The results of this observer will then be presented, along with a comparison between predicted target quantities and the measured ones. Finally, the thesis will conclude with a discussion on how to improve the methods presented and an outlook on future research directions.

Chapter 2

Background

This section is intended to give sufficient technical background knowledge to understand the methods used in this thesis. To get a better understanding of the theory and tools involved it is best to refer to the textbooks, manuals, or works in published journals [8] [23].

2.1 SOLPS-ITER

As was said in the introduction, SOLPS-ITER is a steady-state simulation which means it can only give spatially resolved physical quantities when a plasma is in equilibrium (i.e., static).

Because this thesis aims to take advantage of SOLPS-ITER for time-dependent control, numerous simulations have been done to try and account for the various attop scenarios one can encounter in real experiments. SOLPS-ITER allows a user to specify different parameters which may or may not converge to a solution. Creating many converging solutions with different conditions, allows one to draw conclusions about the steady-state behavior of the system with respect to some sort of actuation. Therefore the main variable which is changed across the simulations used in this thesis are the injection rates of D_2 and N_2. In this way, a map can be made between different injection rates and plasma parameters within SOLPS-ITER. More detail will be given in the Methods section 3, on how SOLPS-ITER is used in this thesis.

2.2 State-Space and Observer

In the introduction it was explained that the task of this thesis is to design an observer. Along with the explanation of the observer there was a repeated reference to a *model*. For this thesis the models will be of a specific form which allows them to be conveniently used with a certain type of observer. This form is discrete-time state-space, and it was will be treated in this section.

$$\begin{aligned} x_{k+1} &= Ax_k + Bu_k \\ y_k &= Cx_k + Du_k \end{aligned} \tag{2.1}$$

On an abstract level, x is a scalar or vector of quantities which change from one discrete time-step k to the next $k+1$ via a linear transformation facilitated by A and B. The u is some input quantity to the system. Meanwhile, the second line is a static linear transformation (i.e., from time k to time k) on the state and input facilitated by C and D. From an engineering perspective this formulation of a model to describe some physically changing state over time, known as state-space, is useful, because it allows for a dynamic part to describe some state transforming over time and some static transformation which can be related to a measurable output.

For example, the dynamics could represent a car where the state is the acceleration and velocity of the car. B might translate a pedal angle$u$ into additional velocity and acceleration of the vehicle

while A translates the current acceleration and velocity x at time k into x at $k+1$. The discrete-time state-space model (of the car) is considered stable if the A is such that it scales the state x down from one time step k to another. If x were just a scalar velocity and A were less than 1, then this would mean the car, without any extra input u would slow down over time. A greater than or equal to 1 would mean the velocity would either remain constant (i.e., never losing momentum) or that it would naturally accelerate: strange situation for a car. For a state with multiple parameters, like a vector with the acceleration and velocity of the car, the analogue of this type of stability is that A must be *Schur*, which essentially means that from one time step to the next the magnitude of the state vector diminishes in magnitude.

Consider then that one can measure the velocity of the vehicle (perhaps using the speedometer and traveling only in one direction) and the acceleration. The model will of course have some errors and so these measurements might serve to correct for these errors. However, like with any measurement device, the sensors are subject to noise. The question naturally arises: what is the best way to use uncertain sensor information and model information to best correct for the model's state?

More specifically, if it is assumed the sensor and the linear time invariant (LTI) model both describe the same underlying true state evolution x, only with additive white noise then there exists an algorithm which can optimally reduce the error between the modeled x and the measured output y: the *Kalman filter*. LTI means A, B, C and D are linear transformations and do not change in time and white noise has zero mean and is statistically independent from one time step to another. More formally, the KF solves the following problem.

A linear discrete-time system with additive white noise on the dynamics and output measurement is given as follows:

$$\begin{aligned} x_{k+1} &= Ax_k + Bu_k + w_k \\ y_k &= Cx_k + v_k \end{aligned} \tag{2.2}$$

The processes $\{w_k\}$ and $\{v_k\}$ are white, zero-mean, uncorrelated with covariance matrices Q_k and R_k, respectively:

$$\begin{aligned} w_k &\sim (0, Q) \\ v_k &\sim (0, R) \\ E[w_k w_k^T] &= Q \\ E[v_k v_k^T] &= R \\ E[w_k v_k^T] &= 0 \end{aligned} \tag{2.3}$$

A Kalman filter (KF) works by making, at each time-step k, a prediction on the state and its covariance at the next time step $k+1$, using measurements taken up until and including time k. In other words, at every time k, the Kalman filter uses an *a priori* estimate (i.e., an estimate prior to the information from a new measurement coming from the previous iteration of the Kalman filter) which is then corrected for by the new measurement information to create the *a posteriori* estimate (i.e., after the measurement is processed. When making the *a posteriori* estimate the difference between the real measurement and the modeled measurement is used as well as a gain (i.e., the Kalman gain) which is calculated at each time step from the covariances of the model uncertainty and the sensor uncertainty. This gain is therefore computed to minimize the covariance between the true state and the estimated state. A diagram detailing this process for one of the models can be seen in 3.4.

This means that the Q and R matrices are directly related to the performance of the KF. Q and R are assumed diagonal for the purposes of this thesis, meaning the noise from one state or output parameter does not affect the other. For simplicity of the explanation here, assume Q and R are not only diagonally but that the trace of Q is all the same number and the trace of R is all the same number. Scaling the trace of of Q relative to R means it is assumed that the true

dynamics processes are subject to a lot more noise than the output measurements. In other words, more trust is given to the output measurements than the modeled state evolution. If the trace of R is much higher relative to Q then more trust is given to the modeled evolution.

Also note that the nature of this algorithm means that the state x does not have to be directly measurable. The KF can simply infer (i.e., reconstruct) what some hidden states might be through the state-space system and the Q and R matrices using measurements from sensors. This can only be done when the system passes the mathematical check of observability: initial states can be uniquely identified from a measured output. Observability will be treated in the context of the models relevant to this thesis in 4.

The Kalman filter is the type of observer which will be employed in this thesis. However, as was just discussed, the Kalman filter needs a model to make predictions and sensors to correct for those predictions. The model will be elucidated upon in the methods section but is based around SOLPS-ITER. The Kalman filter will seek to reconstruct a state defined by SOLPS-ITER based on measurements from real sensors on the TCV. The measurements, therefore, come from real sensors on the TCV and as such an overview of the TCV will be given.

2.3 Le Tokamak a Configuration Variable

The TCV is a tokamak located in Lausanne, Switzerland on the campus of Ecole Polytechnique Federale de Lausanne. The variable configuration moniker is given because of its exceptional number of magnets allowing for a plethora of different plasma configurations.

As the work in this thesis extends on work done by Jesse Koenders [14] [13], and that research was done on the TCV in L-mode, so too will this thesis use TCV shots in L-mode. The table above is given so the reader can gain a better understanding of the operating range of the TCV. It certainly does not reach conditions needed for future power plants (i.e., mainly because the maximum plasma current and magnetic field are too low) but is useful to study in terms of making conjectures about future power plants.

2.3.1 The TCV's Loss Mechanisms

Because of the graphite targets in the TCV, sputtered carbon is usually a major power loss mechanism, accounting for nearly 80% of the total radiated power [24]. However, during Nitrogen seeded scenarios, which are the focus of this research, nitrogen seeding dominates and accounts for 70% of the total radiates power. Because of that fact, having a good idea of the nitrogen density in the vessel is most important when understanding whether the plasma will undergo a radiative collapse in detached regimes.

Figure 2.1: Cross-section of TCV showing the central solenoid, poloidal field coils, and toroidal field coils. Image by M. Toussaint

Operational Parameter	Specification
Major and minor radii	0.88/0.25 m
First wall material	carbon (graphite)
Maximum magnetic field	1.54 T
Maximum plasma current	1.0 MA
Maximum elongation	2.8
Triangularity range	-0.6 / +0.9
Number of toroidal field coils	16
Number of poloidal field coils	16 external (independently powered) + 2 internal
Pulse duration	typ. 2 s, max 4 s
Time between pulses	12'
Main species	H, D, He
Electron density	1-20 10^{19} m^{-3}
Electron temperature	up to 15 keV
Ion temperature	up to 2.5 keV

Table 2.1: Some operational parameter ranges of the TCV experiments from the EPFL wiki. Definitions of these geometric quantities can be found in external resources [8]

Additionally, although volumetric recombination is important on other machines [25], for the TCV, recombination doesn't become an important loss mechanism until after a sufficient decrease in the target ion current and the target temperature [29].

2.4 Gas Valves

There are two gas valves on the TCV which are used in this thesis to actuate the plasma in the divertor: D_2 and N_2. The details of the dynamics of the gas valves are given in [14] and [13]. Both the gas valves are controlled by piezoelectric valves [6]. Additionally, a pressure transducer, located closer to the end of the tube, is used to measure the gas flow in particles per second. Mainly due to the length of this tube and the time delays between requested actuation and real actuation, there is an inherent bandwidth limit on the valves approximately 50Hz on the D_2 valve.

It is important to understand the distinction between the different inputs which relate to the particle influxes from each of the valves. There is a requested gas voltage u_V, a calibrated pressure transducer response u_m directly related to the gas injection rate (also in Volts) and a gas injection rate u_{puff} (in particles per second). For the simplicity of the models in this paper, which are exclusively used offline on prerecorded data, only u_m and u_puff are used, as functions exist for TCV to convert from one to another (again see [13]).

2.5 A Note On Measurement Rate

The rate at which measurements are taken are important for any control system. The simple fact is that if the sampling frequency isn't at least twice the highest frequency of the dynamics being controlled, then critical information is being lost and control might not be possible with such a sensor: the Nyquist-Shannon criterion. Additionally, what frequencies can be controlled is also dependent on how fast the actuation is. For the TCV, considering the time it takes for the gas valves to open, the gas to travel into the vacuum vessel, diffuse into the plasma and the plasma to respond is typically about 15ms [20]. Control engineers usually use a rule of thumb of around at least 8-10 times higher, meaning the sensor should be able to produce a measurement in around 2ms or between 533 and 667 Hz.

This was a deciding factor in choosing certain sensors to be used by the Kalman filter as the use case for this is in a real-time control environment. Note that although the bolometers were initially analyzed due to good agreement with SOLPS-ITER [30] and having a fast sample rate, they were later abandoned for technical reasons B.

2.6 Bolometers

The bolometer system on the TCV is currently a set of 120 sensors located poloidal around the TCV and compromise a third of the types of spectroscopic radiation sensors of the recently installed RADCAM system [22]. Each sensor is a small, gold foil which heats up due to radiation from

The bolometers were chosen because of their high acquisition frequency (around 10kHz for my shots of interest) and therefore their ability to be used in real-time control [22]. Additionally, some of the 120 gold foil sensors [22] pass right through the divertor region which offers a good measurement of photons in the energy range of soft UV and X-rays as well as the kinetic energy from neutrals hitting the surface [25]. In other words, the bolometers allow for line integrated measurements of a lot of the electromagnetic radiation produced by plasma processes as well as energy from neutrals. Typically the bolometers are used to spatially resolve measures of radiated power density (i.e., in W/m^2) by doing tomographic inversions of the sensor measurements offline.

Figure 2.2: A schematic of a gold-foil bolometer sensor

Figure 2.3: The complete RADCAM system including two sensors which are not discussed here, SXR and AXUV. More information can be found in [22].

Attention should be given to the fact that the raw measurements are taken in radiance (i.e., $W m^{-2} sr^{-1}$). The conversion to irradiance (i.e., W/m^2) is dependent on the finite etendue of the sensors as well as the opening of the area in front of the sensors. Although the bolometers were originally used in this thesis, errors were found in both the real data and the synthetic diagnostic:

see the appendix for more details B. Also to note in the appendix is a discrepancy that was found in the data which lead to the realization that for the shots of interest to this thesis (i.e., those used in [13]), the data was not calibrated and therefore could not be used.

2.7 MANTIS and y_{NII}

MANTIS stands for Multispectral Advanced Narrowband Tokamak Imaging System. It is multispectral in the sense that it has 10 different cameras which each capture a different wavelength of light corresponding to a narrow bandwidth of about 1 nm [25]. This means each channel can only adequately cover a single atomic transition. MANTIS receives incoming light from a perspective looking toroidally down the TCV vacuum vessel.

Because of this perspective on the divertor region, algorithms have been introduced to spatially resolve radiation points for real-time control [19]. Functionally these algorithms take the spectra from MANTIS to identify a bulk of radiation along the outer divertor leg of the TCV. Then, arbitrarily, 50% of the maximum brightness point of this bulk, relative to the distance from the target, is located also known as the 50% extinguish front. Throughout this thesis, this will often just be referred to as the CIII or NII front, as these are the two species of interest, and the 50% extinction front is the only extinction front percentage considered. CIII is the radiation from Carbon missing two electrons and NII is the radiation from Nitrogen missing one electron. In literature the 50% extinction front is also referred to generically, for any species, as L_{pol} [19].

The NII and CIII fronts have been studied with NII representing a cooler plasma region than CIII as NII radiates in cooler conditions than CIII. The locations of these fronts along the divertor leg are of particular interest because they have been shown to correlate strongly with the target temperature [25] [14]. In essence, because certain electromagnetic spectra coincide with specific temperatures, which are themselves dependent on processes caused by injecting impurities, engineers can use the location of the emission fronts (i.e. L_{pol} generally and y_{NII} specifically) to describes regimes when conditions are favorable for the target. For example, if the temperature is low enough in the divertor region for the NII front to radiate, then it is known that this region has an electron temperature of about 6.5ev [24], meaning other radiative processes such as volumetric recombination can begin to occur.

Left: a schematic of a poloidal view of the TCV with a magnetic equilibrium reconstruction of the field lines in blue. In addition, the approximate locations of N_2 and D_2 gas injections are shown in green as well as the central FIR chord. Right: Spatial emissivity plot from MANTIS showing the y_{NII} 50% extinction front location along the outer divertor leg at different times in an experiment on TCV marked as a cyan . From [12]

a shows a schematic of a poloidal view of the TCV with a magnetic equilibrium reconstruction of the field lines in blue. The port location is illustrated between a and b. b shows the toroidal perspective that MANTIS has on the TCV. From [19]

2.8 FIR

The FIR 2.4a measures line-integrated electron densities by using interferometry lines which shine vertically down through the vacuum vessel of the TCV. The electron density in the plasma a ects the phase of the beams emitted through the plasma. This phase is compared to a reference beam and an estimate can then be made of the line-averaged electron density.

It was implemented in the 2023 paper by Koenders [12] to perform MIMO control using the D_2 and N_2 gas valves. The central chord of the FIR lines is indicative of fusion power conditions in the core and therefore the power entering the SOL.

More detail can be found in [7], but as this sensor is not directly used in this research, the explanation given here should su ce.

2.9 VIR

The vertical infrared camera, or VIR on the TCV, is a CMT 256 M HS Thermosensorik Infrared Camera, mounted to look vertically down on the plasma. This gives it a view of the graphite tiles on the bottom of the TCV and therefore insight into the heat ux deposited on the outer divertor target on the TCV.

It has a relatively fast acquisition frequency of 178Hz, but to compute the perpendicular heat ux, among other computational steps, a 2D heat conduction equation with speci c boundary conditions must be solved. Due to this frequency limitation, this sensor is therefore not used with the KF, but instead is used to validate the results of using the KF. It will show how well the SOLPS-ITER parameters reconstructed by the KF correlate to the maximum perpendicular heat ux.

Figure 2.5: Poloidal schematic showing the vantage point of the VIR from the EPFL wiki

Chapter 3

Methods

This section is to serve as a means of motivating, and for the reader, reproducing, what was done to get the results presented in the next chapter. The bigger picture is that a Kalman filter is to be used to reconstruct state parameters defined by SOLPS-ITER. Therefore it will first be discussed what states will be chosen. After, an explanation of how these states relate to a range of SOLPS-ITER simulations will be given. Finally, the method of leveraging static SOLPS-ITER simulations for a dynamic model and its use in a Kalman filter will be elucidated.

In addition, a method using the model identified in [12], in combination with a KF, will be employed in creating some relationship to the defined state parameters from the previous model and the diagnostics used: the CIII and NII front as measured by MANTIS. This is another method employed in this thesis to relate a dynamic model to some of the steady-state information in SOLPS-ITER.

It is important to remember that the motivation for reconstructing SOLPS-ITER parameters is to correlate these states with conditions at the target. This is essential if it is desired to use the model for some type of Model Predictive Controller to try and predict future target conditions and stop unwanted ones before they occur. As such the method for correlating the KF's reconstructed SOLPS-ITER parameters with the divertor target parameters will be given.

3.1 Motivating the Choice of State

Because detachment (i.e., a state in the divertor region characterized by considerably lower target temperatures and heat fluxes) is directly related to the injection of colder gasses (i.e., fueling and impurity), it is natural for the state parameters to be both a reflection of the degree of detachment and dynamically related to the injection of the gasses. Two candidate parameters have been researched at DIFFER on the basis of the aforementioned criteria: impurity density and neutral pressure.

For the TCV, the impurity gas that is injected is N_2 and therefore the state parameter would be nitrogen density: n_N. Ideally the evolution of n_N in the vessel is just degree of integration of nitrogen over time as gas is injected in and pumped out at some rate. Because the impurity content plays a large roll in radiating power away from the divertor (e.g., via line radiation 2) n_N is related to the temperature, and heat-flux that the target experiences. Again, comprising 70% of the total integrated power in Nitrogen seeded shots [24]. It should also be noted that n_N in this thesis is defined as the density of all species of nitrogen (i.e., nitrogen in all its forms of ionization and as a neutral).

Neutral pressure, p_0, is dependent on neutral temperature and neutral density. Neutral pressure increases in the TCV as more gasses are injected, either D_2 or N_2, or if ionized gasses recombine (e.g., hydrogen, nitrogen, oxygen, carbon or helium). This recombination mainly happens [25] as ions lose energy from ion-neutral collisions, volumetric recombination, line-radiation and therefore is a good indicator of the conditions at the target. It should be noted that volumetric recombination

has not been found to play a large role in detachment on the TCV [25] and is therefore an exception with regards to other tokamaks. In essence, as neutral pressure increases, it indicates both that more gasses are being injected (i.e. N_2 and D_2) and of an environment in which more ions can radiate power away before depositing power on the divertor target. It is assumed that p_0 sees greater dynamic changes from the injection of N_2 and D_2 because of much weaker variations in neutral temperature. It is difficult to verify this experimentally as T_0 cannot be directly measured, but this will be shown to be a good assumption with respect to SOLPS-ITER.

As was discussed earlier, these states must be able to be defined in SOLPS-ITER as SOLPS-ITER contains information about the target parameters which should be able to be correlated with the state: n_N and p_0. Because SOLPS-ITER represents physical quantities spatially resolved over a 2-D poloidal view of the TCV, it becomes a question of which n_N and p_0 to choose over the area of the divertor region. This will be discussed in the coming section 3.4.

3.2 Experiments Used

The six shots that were investigated are the same as the L-mode discharges used in [13]: #68861, #69147, #69144, #69185, #69145, and #69148. These are shots with a plasma current of 340 kA and a toroidal magnetic field of 1.4 T, as well as a line-averaged electron density of $\bar{n}_e$ 9 $10^{19} m^{-3}$.

3.3 SOLPS-ITER Simulations Used

D_2 # N_2 !	0e20	1e20	2e20	3e20	4e20	5e20	8e20	12e20
2.5e20	127676	127683	127690	127697	127705	127712	127719	127726
5e20	127677	127684	127691	127698	127706	127713	127720	127727
7.5e20	127678	127685	127692	127699	127707	127714	127721	127728
10e20	127679	127686	127693	127700	127708	127715	127722	127729
12.5e20	127680	127687	127694	127701	127709	127716	127723	127730
15e20	127681	127688	127695	127702	127710	127717	127724	127731
17.5e20	127682	127689	127696	127703	127711	127718	127725	

Table 3.1: The 55 SOLPS-ITER simulations used. Each simulation's MDS (fusion database) number corresponds with their respective inputs of D_2 and N_2 in particles per second. A complete list of the loss mechanisms present in these simulations can be found in [25].

The state parameters should be based on quantities extant in SOLPS-ITER simulations in some capacity as these parameters will be reconstructed from real measurements on the TCV via the Kalman filter. The SOLPS-ITER simulations chosen should therefore reflect the operational space of the experiments with which comparisons will be done. This operational space should therefore be based on the shots done in [13] as these were experiments in which divertor control on the TCV was tested. The data from these shots are appropriate to use for this research as the Kalman filter will be developed for a control system for the TCV divertor.

As is stated in [30], it can be difficult to make direct comparisons between SOLPS-ITER and real experiments. Much of this is inherently tied to the steady-state nature of SOLPS-ITER and therefore trying to make comparisons to dynamic experiments is only, arguably, possible under certain conditions (e.g., linear density ramps [25] [30]). Research is still ongoing on how to reconcile specific differences between SOLPS-ITER simulations and analogous quantities measured on the real TCV. In that sense, using SOLPS-ITER simulations to represent the dynamics of the SOL of the real TCV should be seen as experimental and it should not be surprising if differences persist in the validation section 4.

For the purposes of this thesis, SOLPS-ITER simulations were chosen which cover most of the range of the injection rates in the experiments done in [13]: experiments #68861, #69147,

#69144, #69185, #69145, and #69148. The simulations also use a wall recycling coe cient of 0.5 which agrees with the measured recycling coe cient on TCV [24].

The table above 3.1 organizes the SOLPS-ITER simulations based on their injection rates. The power entering the SOL, as calculated by integrating the radial heat ux in the SOLPS-ITER simulation at the separatrix, has an average of 410.22 kW and a standard deviation of 6.7368 kW. This means that the SOLs in these simulations are subjected to roughly the same conditions from the core. This is important because it allows for a better comparison of the SOLs which are subject to di erent fueling and impurity injections. The upstream conditions (i.e., further away from the target along the SOL) of the SOLPS-ITER simulations are also similar to experiment in that their outer-midplane separatrix electron densities are similar to this same quantity as measured by Thomson Scattering. The outer-midplane refers to an arbitrary point upstream along the separatrix on the low- eld side of the tokamak. Taken at an arbitrary attop time of about 1.5 seconds, the mean and standard deviation of the $n_e^{sep;omp}$ across the six shots used are compared with the mean and standard deviation of the analogous SOLPS-ITER simulation values:

	$n_e^{sep;omp}$	
SOLPS-ITER	2.9799e+19	9.6648e+18
Experiments	2.0483e+19	4.2962e+18

Table 3.2: Comparing the averaged outer-midplane electron density on the separatrix across the SOLPS-ITER simulations and experiments #68861, #69147, #69144, #69185, #69145, and #69148. The experiments used Thomson Scattering measurements to obtain an estimate on $n_e^{sep;omp}$.

3.4 Leveraging SOLPS-ITER for a Dynamic Model

Before beginning this section, it is helpful to rst note that leveraging SOLPS-ITER simulations will involve taking into account two aspects of SOLPS-ITER:

- Capturing the steady-state condition
- Capturing the diagnostic relationships via static maps

What these two conditions mean in practice will be the subject of this section.

3.4.1 Steady-State Condition and State-Space Model

Because it is intended for the Kalman lter to reconstruct a state from SOLPS-ITER simulations, n_N and p_0 must be de ned via SOLPS-ITER simulations. As was stated at the beginning of the methods section, the spatial nature of SOLPS-ITER necessitates choosing a speci c region in two-dimensional poloidal space where values for n_N and p_0 are de ned.

It was decided to take an average of n_N and p_0 over a poloidal region of SOLPS-ITER simulations as it was thought that these parameters must, on average over the space, match physical reality. In other words, it is less likely that a single cell in SOLPS-ITER simulations of the TCV of n_N or p_0 would match a real experiment. This, however, leaves an extremely large, but nite set of cells which can be averaged over to de ne the SOLPS-ITER state parameters n_N and p_0. More precisely, because each cell in SOLPS-ITER can be used or not used then this means there are 2^{3332} combinations of cells to choose from. Therefore an additional condition was imposed on which areas could be averaged over: those areas which give a su ciently linear steady-state condition. This imposition is justi able as the dynamic model is chosen to be linear for the purposes of being able to capture the steady-state behavior of SOLPS-ITER in the model. An extra constraint was added that only cells in the divertor region are relevant for observing the divertor region. Further, these choices of area-averaged n_N and p_0 should give a linear steady-state condition with respect

Figure 3.1: A grid of the 55 SOLPS-ITER simulations used in this thesis of the two parameters n_N and p_0. This can be used as a reference for how these parameters vary spatially across di erent SOLPS-ITER simulations.

to gas injections as linear dynamics are desired for the linear KF. So, before revealing the how n_N and p_0 are spatially de ned, the steady-state condition taht SOLPS-ITER de nes must rst be discussed.

To de ne this steady-state condition, the form of the discrete-time state-space model must be discussed. This model is based on simple assumptions about how the neutral pressure and nitrogen density evolve in the divertor region.

$$\begin{aligned} x_{k+1} &= \begin{bmatrix} A_{11} & 0 \\ 0 & A_{22} \end{bmatrix} \begin{bmatrix} n_N \\ p_0 \end{bmatrix} + \begin{bmatrix} B_{11} & B_{12} \\ B_{21} & B_{22} \end{bmatrix} \begin{bmatrix} 0 & 0 \\ 0 & 1 \end{bmatrix} \begin{bmatrix} \Gamma_{N_2} \\ \Gamma_{D_2} \end{bmatrix} \\ y_1 \\ y_2 &= \begin{bmatrix} C_{11} & C_{12} \\ C_{21} & C_{22} \end{bmatrix} \begin{bmatrix} n_N \\ p_0 \end{bmatrix} + \begin{bmatrix} 0 & 0 \\ 0 & 0 \end{bmatrix} \begin{bmatrix} D_{13} & 0 \\ 0 & D_{24} \end{bmatrix} \begin{bmatrix} \Gamma_{N_2} \\ \Gamma_{D_2} \end{bmatrix} \end{aligned} \tag{3.1}$$

As gas is injected into the vessel, the nitrogen in ux is integrated over time and builds up in the divertor region as it is being pumped out. From one time step to another, the previous n_N in the divertor region a ects the next n_N. It is assumed that only the in ux of N_2 will an e ect of n_N. The dynamics for p_0 are de ned by similar assumptions: a ected by $_{N_2}$ and $_{D_2}$ and integrated over time. It is important to note that integration here does not refer to a pure integration, but some degree of integration from one time sample to the next which is dependent on the values in the A matrix. It is also important to note that the subscripts of the letters within the matrices simply refer to the row and column positions of the values contained within the matrices.

The input is augmented with ones, so that linear o sets in the output mappings could be considered. The output will be discussed in the next subsection.

That is, when mapping from $_{D_2}$ and $_{N_2}$ to some choice of area-averaged n_N and p_0 over all 55 of the SOLPS-ITER simulations, how well does a linear t approximate this mapping? Through trial and error, regions for n_N and p_0 in the divertor region of SOLPS-ITER were found which give su ciently good linear maps from the system inputs. The maps were created via linear least-squares tting and so su ciently good was dictated by a compromise of a su ciently high R-squared value (& 0.9) and time spent on the trial and error. Perhaps better regions could be chosen via some optimization algorithm, but that was deemed outside the scope of this thesis.

To capture the steady-state condition as a relationship between A and B, it is helpful to use the following expression for the steady-state condition of any discrete time LTI state-space model:

$$x_{ss} = (I \quad A)^{\ 1} B u_{ss} \tag{3.2}$$

This shows the relationship between the steady-state gas in uxes u_{ss} from, for example, the SOLPS-ITER simulations to the steady-state state n_N and p_0. This allows one to express the steady-state condition as a relationship between A and B. For the model in question 3.1, under the imposition of 3.2 the equations below result.

$$\begin{aligned} B_{22} &= \frac{p_0}{_{D_2}}(1 \quad A_{22}) \\ B_{11} &= \frac{n_N}{_{N_2}}(1 \quad A_{11}) \\ B_{21} &= \frac{p_0}{_{N_2}}(1 \quad A_{22}) \end{aligned} \tag{3.3}$$

The fractions in the above set of equations are the linear mappings from the inputs to the states. For example, $\frac{n_N}{_{N_2}}$ is the best- t slope which relates $_{N_2}$ to n_N for the 55 SOLPS-ITER simulations available.

Figure 3.2: The regions in SOLPS-ITER over which the states n_N and p_0 are averaged. This is an example from SOLPS-ITER simulation with MDS number 127719

3.4.2 Relationship to Diagnostics

The outputs y in 3.1 are related to SOLPS-ITER synthetic diagnostics. The synthetic diagnostic used for this model could represent SOLPS-ITER versions of any sensors on the TCV which are hopefully responsive to gas valve actuation. However, in the case of this thesis, only the CIII and NII fronts were investigated whose real analogue is measured by MANTIS. These synthetic diagnostics were chosen as they have shown potential in previous research with respect to real experiments [25] [13]. These experiments show MANTIS is fast enough for the real-time control of the divertor region using gas injection on the TCV and that MANTIS's analogous SOLPS-ITER front measurements are useful in real TCV modeling scenarios. For example, in [14] the steady-state condition for the control-oriented model is derived from SOLPS-ITER simulations and measurements of the CIII front.

Using functions used in [13], synthetic CIII measurements were generated for all 55 simulations. The Matlab function for computing the NII front location was developed for this thesis and is based almost entirely on the function which computes the CIII front location from SOLPS-ITER. This function was used to compute NII front locations for each SOLPS-ITER simulation. Then, linear least squares tting was employed to correlate the statex (i.e., n_N and p_0) to these synthetic outputs.

$$\begin{bmatrix} y_{CIII} \\ y_{NII} \end{bmatrix} = \begin{bmatrix} C_{11} & C_{12} \\ C_{21} & C_{22} \end{bmatrix} \begin{bmatrix} n_N \\ p_0 \end{bmatrix} + \begin{bmatrix} 0 & 0 & D_{13} & 0 \\ 0 & 0 & 0 & D_{24} \end{bmatrix} \begin{bmatrix} 2 \\ 6 \\ 6 \\ 4 \end{bmatrix} \begin{matrix} 3 \\ n_{N_2} \\ n_{D_2} \\ 1 \\ 1 \end{matrix} \begin{matrix} 7 \\ 7 \\ 5 \end{matrix} \tag{3.4}$$

Because these ts were allowed a linear o set (i.e., the planes were regressed using the form $y = C_{11}\ n_N + C_{21}\ p_0 + D_{13}$), the input was augmented with ones to allow for this o set to express

(a) $n_N[10^{18}] = 0:16341\ {}_{N2}[10^{20}]$. The coe cient has a standard error of 0.0014. The t has an R-squared value of 0.99.

(b) $p_0 = 0:016147\ {}_{N2}[10^{20}] + 0:057679\ {}_{D2}[10^{20}]$. The coe cients have standard errors of 0.0018 and 0.00092 respectively. The t has an R-squared value of 0.9493.

Figure 3.3: Two linearly-regressed ts which describe the steady-state relationship between the gas pu s u and the state x over the 55 SOLPS-ITER simulations. Notice the 55 red dots in each plot.

itself in the values of D_{13} and D_{24}.

An example output is given above in 3.4 where, because the output is chosen as the synthetic CIII and NII front position, the top row of C and D correspond to the linearly regressed t for the position of the CIII front over all 55 simulations. The same is true for the NII front position but with the second row of C and D.

3.5 Using a Transformed Di usion Model

Another method for relating a dynamic model to SOLPS-ITER is to use a model that has already been validated in control experiments. The model in question is from [12] and relates the gas in uxes to a a measure of the line-integrated electron density via the FIR and the position of the 50% NII extinction front along the outer leg measured by MANTIS. It is a MIMO model of the form:

$$\begin{matrix} x_{NII}(s) \\ x_{hn_{e}i_{l}}(s) \end{matrix} = \begin{matrix} G_{y_{NII};D2} & G_{hn_{e}i_{l};D2} \\ G_{y_{NII};N2} & G_{hn_{e}i_{l};N2} \end{matrix} \begin{matrix} u_{m;D2}(s) \\ u_{m;N2}(s) \end{matrix} \tag{3.5}$$

Where the Gs are di erent variations of the following non-rational transfer function which describes di usion processes.

$$x(s) = \frac{\cosh(\hat{x}\ )\tanh(L\ ) \quad \sinh(\hat{x}\ )}{D} u_m(s): \tag{3.6}$$

The SOLPS-ITER simulations can be used again here to generate a static transformation between quantities. In this case a static transformation between the 50% extinction front of NII and the line integrated electron density of the central FIR chord to n_N, and p_0. This transformation is accomplished via linear regression between synthetic diagnostic versions of the FIR and MANTIS over the 55 simulations.

First, the transformation matrix T 3.11 needed to be created from the 55 simulations. This was done by organizing the data into matrices where each column is data from a di erent SOLPS-ITER simulation and pre-multiplying them by scaling factors such that the matrix inverses are

not ill-conditioned. In other words, if X was not scaled by then taking the Penrose inverse$^+$ would be ill-conditioned.

It is important to note that although there is a synthetic diagnostic for the FIR available from the researchers at the EPFL, this comes with inherent inaccuracies because the central FIR chord passes through the core and SOLPS-ITER does not simulate the core. Therefore, a linear scaling multiplication of 10 was used to attempt to compensate for this as it was noticed that the simulations were approximately a factor 10 o from the experiments being used. This means $\langle n_e \rangle_l$ in the following matrices are actually 10 times greater than what comes from the evaluation of this synthetic diagnostic.

Relationships between $n_e^{sep;omp}$ and central FIR chord's $\langle n_e \rangle_l$ were investigated over the six experimental shots, in order to make a transformation between the analogous SOLPS-ITER parameters, but such a methodology did not yield the same clear results as is seen in [30]. The authors of [30] point out that this method only really applies for a clear density ramp and the six shots explored in this thesis do not have consistent density ramps in D_2 and N_2.

$$= \begin{matrix} 1 & 0 \\ 0 & 10^{18} \end{matrix} \tag{3.7}$$

$$= \begin{matrix} 10^{18} & 0 \\ 0 & 1 \end{matrix} \tag{3.8}$$

$$X = \begin{matrix} y_{NII}^1 & \cdots & y_{NII}^i \\ \langle n_e \rangle_l^1 & \cdots & \langle n_e \rangle_l^i \end{matrix} \tag{3.9}$$

$$Y = \begin{matrix} n_N^1 & \cdots & n_N^i \\ p_0^1 & \cdots & p_0^i \end{matrix} \tag{3.10}$$

$$T = Y X^+ \tag{3.11}$$

Then, the parts of the MIMO model presented in [12] can be transformed. Below, $G_{y_{NII};N_2}$ corresponds to the dynamics between injecting N_2 and the response of the NII front, while $G_{\langle n_e \rangle_l;D_2}$ represents the dynamic response between the injection of D_2 gas and the central FIR chord line-integrated electron density.

$$^1T \begin{matrix} G_{y_{NII};D_2} \\ G_{\langle n_e \rangle_l;D_2} \end{matrix} = \begin{matrix} G_{n_N;D_2} \\ G_{p_0;D_2} \end{matrix} \tag{3.12}$$

$$^1T \begin{matrix} G_{y_{NII};N_2} \\ G_{\langle n_e \rangle_l;N_2} \end{matrix} = \begin{matrix} G_{n_N;N_2} \\ G_{p_0;N_2} \end{matrix} \tag{3.13}$$

A MIMO transfer function can then be reconstructed with these new G matrices.

$$\begin{matrix} G_{n_N;N_2} & G_{p_0;N_2} \\ G_{n_N;D_2} & G_{p_0;D_2} \end{matrix} \tag{3.14}$$

Then this MIMO transfer function can be converted to a state-space model which can actually be used by the Kalman lter.

$$\begin{aligned} x_{k+1} &= A\tilde{x}_k + B\begin{matrix} & 0_{80\ 2} \end{matrix} u_k \\ y_k &= C\tilde{C}\tilde{x}_k + D u_k \end{aligned} \tag{3.15}$$

By making the linear transformation from Koenders' choice of diagnostics [12] to n_N and p_0, a new state space is de ned which is distinguished in the above state-space model 3.15 by the . For the clarity of the reader, this model will be referred to as Koenders' Transformed Model (KTM), for the name to refer to its origins.

The input is an augmented form of u_m (V), as u_m is what Koenders' model originally uses. Because of this augmentation, zeros are appended to B. The reason for such large dimensions of A, B and C is because they come from a decomposition process of the original MIMO di usion model [12] to describe with state-space matrices.

$$u = \begin{bmatrix} u_{m;N_2} \\ u_{m;D_2} \\ 1 \\ 1 \end{bmatrix}$$

The C and D in 3.15 are simply the same as in 3.1 (i.e., the transformation to some synthetic diagnostic from n_N and p_0).

Again, any diagnostic which meets the requirements of being sensitive enough to gas injections, measures fast enough, and can be synthetically computed in SOLPS-ITER could decide the C and D matrices. However, this thesis will focus on the C and D which relate n_N and p_0 to the CIII and NII front locations.

It is important to note that that the state x is a set of 80 parameters which come from the transformed version of an approximation of the non-rational di usion transfer function from [13].

3.6 Kalman lters

Because there are two approaches to using models to relate dynamics to SOLPS-ITER parameters, there will therefore be two Kalman lters. Again, these Kalman lters will be used to reconstruct a state based on repeatedly updating predictions made on the output using real-time measurements. The resulting reconstructed state or output therefrom in the case of Koenders' Transformed Model will then be correlated with SOLPS-ITER parameters which are critical to the target.

3.6.1 Integration Model

For the integration model the Kalman lter prediction step looks like:

$$\hat{x}_{k+1|k} = \begin{bmatrix} A_{11} & 0 \\ 0 & A_{22} \end{bmatrix} \begin{bmatrix} \hat{n}_N \\ \hat{p}_0 \end{bmatrix}_{k|k-1} + \begin{bmatrix} B_{11} & 0 & 0 & 0 \\ 0 & B_{22} & 0 & 0 \end{bmatrix} \begin{bmatrix} u_{m;N_2} \\ u_{m;D_2} \\ 1 \\ 1 \end{bmatrix}_k \tag{3.16}$$

$$\begin{bmatrix} \hat{y}_1 \\ \hat{y}_2 \end{bmatrix}_{k|k} = \begin{bmatrix} C_{11} & C_{12} \\ C_{21} & C_{22} \end{bmatrix} \begin{bmatrix} \hat{n}_N \\ \hat{p}_0 \end{bmatrix}_{k|k-1} + \begin{bmatrix} 0 & 0 & D_{11} & 0 \\ 0 & 0 & 0 & D_{22} \end{bmatrix} \begin{bmatrix} u_{m;N_2} \\ u_{m;D_2} \\ 1 \\ 1 \end{bmatrix}_k \tag{3.17}$$

Here the hats mean that this it is an estimated variable by the Kalman lter. Also, the subscripts are to clarify at what time step the state is being estimated and with how much previous information it has collected to make this estimate. For example, $k+1|k$ means an estimate of what the state will be at $k+1$ using the previous $k-1$ iterations of the Kalman lter and sensor measurements.

The correction step looks like:

$$\begin{aligned} P_{k+1|k} &= AP_{k|k}A + Q \\ M_k^x &= P_{k|k-1}C^T/(CP_{k|k-1}C^T + R) \\ \hat{x}_{k|k} &= \hat{x}_{k|k-1} + M_k^x(y_k - C\hat{x}_{k|k-1} - Du_k) \\ \hat{y}_{k|k} &= C\hat{x}_{k|k} + Du_k \end{aligned} \tag{3.18}$$

The initial condition for the error covariance matrix $P_{0|0}$ is AQA because the noise is additive with respect to the state dynamics. The initial state x_0 is set to 0 for simplicity.

Additionally, a constraint is added to the algorithm which saturates for negative state predictions (i.e., one can only have, at the very smallest, 0 density and pressure). This is modeled choosing the minimum of 0 and the filtered state value.

It can be difficult to understand the recursive nature of the Kalman filter without thinking about it computationally, so the loop is given in a diagram 3.4. Note that the constraint is not included in this diagram. Notice that the entire KF exists within a region where all state, input, and output, are all made to be roughly on the same scale. This is important so the matrix inverses inolved in the KF are not ill-conditioned.

3.6.2 Koenders' Transformed Model

For Koenders' Transformed Model the Kalman filter prediction step looks like:

$$\begin{aligned} \hat{x}_{k+1|k} &= \tilde{A}\hat{x}_{k|k-1} + \tilde{B}u_k \\ y_{k|k} &= \tilde{C}\tilde{C}x_{k|k-1} + Du_k \end{aligned} \tag{3.19}$$

The correction step looks like:

$$P_{k+1|k} = \tilde{A}P_{k|k}\tilde{A}^T + \tilde{Q} \tag{3.20}$$

$$M_k^x = P_{k|k-1}(\tilde{C}\tilde{C})^T/((\tilde{C}\tilde{C})P_{k|k-1}(\tilde{C}\tilde{C})^T + \tilde{R}) \tag{3.21}$$

$$\hat{x}_{k|k} = \hat{x}_{k|k-1} + M_k^x(y_k - (\tilde{C}\tilde{C})\hat{x}_{k|k-1} - Du_k) \tag{3.22}$$

$$P_{k|k} = (I - M_k^x)P_{k|k-1} \tag{3.23}$$

Notice that the Kalman filter update step uses $\tilde{C}\tilde{C}$ to reconstruct the state. This implies that the Kalman filter is not only using Koenders' Transformed Model to reconstruct the state, but also the synthetic diagnostics from SOLPS-ITER defined by the $\tilde{C}$ matrix. The $\tilde{Q}$ and $\tilde{R}$ matrices will be shown how to be tuned in the results section.

Figure 3.4: KF algorithm

3.7 Validation

It is not trivial to validate the time evolution of states that are not directly measurable. However, since the purpose of the Kalman filter is to reconstruct SOLPS-ITER parameter which are to be correlated with other SOLPS-TIER, a comparison can be made to target parameters of interest as well as a different SOLPS-ITER parameter which is measurable.

The target parameters that will be investigated are the following maximal quantities across the outer divertor target: perpendicular heat flux, electron temperature, and perpendicular ion flux. These are important quantities to investigate as they can be used in future applications of the Kalman filter in conjunction with some type of controller which can consider critical divertor target constraints.

The time series SOLPS-ITER approximation of the maximal perpendicular heat flux at the outer target will be compared to a measurement done by the VIR. Then the other two SOLPS-ITER approximations of the aforementioned target quantities can be validated by comparing what value for the maximal perpendicular heat flux results from the two given the following relation.

$$q_t = \gamma_t (T_e + E_{pot}) \tag{3.24}$$

Here the sheath heat transmission coefficient is taken to be 5 for the TCV [25]. E_{pot} is the potential energy of recombination with respect to the plasma and the surface. Stangeby in [26] breaks the potential down as $E_{e\ i}^{surface\ \ recomb} + E_{atom\ \ atom}^{surface\ \ recomb}$ which is approximately said to be 15eV. However, to be more precise, this potential is 13.6eV + 1.1eV [27][pg. 653] where the assumed ion reflection coefficient is 0.5. It should be noted that this differs from [28], but the difference is minor and still puts E_{pot} around 15eV.

In summation, the validation process is a means to check to what degree the process of correlating the reconstructed KF SOLPS-ITER state parameters can predict real-life, measurable analogues on the TCV.

Chapter 4

Results

The results of using the previous section's methods are applied here on the TCV experiments: #68861, #69147, #69144, #69185, #69145, and #69148. Only #69145 and #69148 are shown in the results and the rest are left to the appendix for ease of reading. #69145 and #69148 are given priority for the reader because these shots involved following a more aggressive step reference by actuating just $_{N_2}$ (i.e., #69145) and just $_{D_2}$ (i.e., #69148). In theory, this should be a more challenging reference for the KF to follow than the references from the other shots and therefore is a better indication how it might perform in the worst case. These are the same shots used in [13] for identi cation and control of the divertor plasma dynamics in TCV. The two shots presented in [12] were not used because the CIII and NII front data for these experiments could not be found.

4.1 Steady-State Fits and the Integration Model

Through hand-tuning the A and B of the discrete model 3.1 based on a basic intuition of integration and how the model responded in tandem with a Kalman lter, the following state-space model was realized:

$$\begin{aligned}
\begin{bmatrix} n_N & 10^{18} \\ p_0 & \end{bmatrix}_{k+1} &= \begin{bmatrix} 0:9997 & 0 \\ 0 & 0:99995 \end{bmatrix} \begin{bmatrix} n_N & 10^{18} \\ p_0 & \end{bmatrix}_k \\
&\quad + \begin{bmatrix} 4:90 & 10^{5} \\ 8:10 & 10^{7} \end{bmatrix} \begin{bmatrix} 2^{k} & \\ & 2:88 \quad 10^{6} \end{bmatrix} \begin{bmatrix} 0 & 0 \\ 0 & 0 \end{bmatrix} \begin{bmatrix} 6 & 6 \\ 4 & \end{bmatrix} \begin{bmatrix} N_2 & 10^{20} \\ D_2 & 10^{20} \end{bmatrix} \begin{bmatrix} 3 \\ 7 \\ 5 \end{bmatrix} \\
\begin{bmatrix} y_{CIII} \\ y_{NII} \end{bmatrix}_k &= \begin{bmatrix} 0:0514 & 02952 \\ 0:0510 & 03082 \end{bmatrix} \begin{bmatrix} n_N & 10^{18} \\ p_0 & \end{bmatrix}_k \\
&\quad + \begin{bmatrix} 0 & 0 \\ 0 & 0 \end{bmatrix} \begin{bmatrix} 0:0150 & 0 \\ 0 & 0:0519 \end{bmatrix} \begin{bmatrix} 2^{k} & \\ & 6 \\ & 4 \end{bmatrix} \begin{bmatrix} N_2 & 10^{20} \\ D_2 & 10^{20} \end{bmatrix} \begin{bmatrix} 3 \\ 7 \\ 5 \end{bmatrix}_k
\end{aligned} \tag{4.1}$$

The model inputs and states are scaled such that they are on a similar scale as the least-squares ts for the C and D matrices as well as the least-squares ts used to derive the steady-state condition for A and B. These least-squares ts needed to be scaled to ensure that the squared di erence could be minimized between, for example, n_N on the scale of 10^{18} and p_0 on the scale of 1. Consider also that the Kalman lter performance degrades or can become entirely impossible if the matrix inverses involved in the algorithm are ill-conditioned (e.g., contain numbers of drastically di erent magnitudes).

(a) $n_N[10^{18}] = 0.16341\ {}_{N_2}[10^{20}]$. The coefficient has a standard error of 0.0014. The fit has an R-squared value of 0.99.

(b) $p_0 = 0.016147\ {}_{N_2}[10^{20}] + 0.057679\ {}_{D_2}[10^{20}]$. The coefficients have standard errors of 0.0018 and 0.00092 respectively. The fit has an R-squared value of 0.9493.

Figure 4.1: Two linearly-regressed fits which describe the steady-state relationship between the gas puff u and the state x over the 55 SOLPS-ITER simulations. Notice the 55 red dots in each plot.

The discrete-time steady-state formalism 3.2 can be filled in with the slopes from the least-squares fitted functions 4.1.

$$\begin{matrix} 10^{18} & 0 \\ 0 & 1 \end{matrix} x_{ss} = \begin{matrix} 0.16341 & 0 & 0 & 0 \\ 0.016147 & 0.057679 & 0 & 0 \end{matrix} u_{ss} \quad 10^{20} \tag{4.2}$$

Again, the discrete-time steady-state formalism can be rewritten as a series of equalities 3.3.

$$\begin{aligned} B_{22} &= 0.057679(1 - A_{22}) \\ B_{11} &= 0.16341(1 - A_{11}) \\ B_{21} &= 0.016147(1 - A_{22}) \end{aligned} \tag{4.3}$$

These equality constraints were used such that the just the system's A matrices could be tuned and the B matrix would follow dependently. These equality constraints could be used in an algorithm to find an optimally tuned A and B with fixed C and D C.

As the FIR was initially considered to be used in the Kalman filter, the sample frequency for this system is the same as the FIR: 25kHz. Because the FIR could potentially be used in future iterations of the Kalman filter, and 25kHz is well above the Shannon-Nyquist criterion of twice the highest frequency in any other sensor used in this thesis, the 25kHz remains. The interpolation method that was used was simply a zero-order hold using MATLAB's `interp1()` function with the `'previous'` option.

The system 4.1 is still observable, controllable, and Schur stable 2, meaning it meets the theoretical minimum to use in the context of control applications.

4.2 Synthetic Diagnostic Fits

To derive C and D, static fits were made between the state parameters and the position of the NII and CIII 50% extinction fronts in the outer divertor over the 55 SOLPS-ITER simulations. These locations can be directly compared to what MANTIS might measure for the same quantities. For the CIII front this is the same synthetic diagnostice used in [14]. An analogue of this diagnostic was created for the NII front location similarly using emission values extracted from the ADAS database

[1]. This leads to a slight discrepancy between the real MANTIS measurement of 399.5nm and the synthetic one measuring 399.610nm. However, as seen in [13], the dynamics between di erent emission fronts are relatively similar, but only having a slight o set. It is therefore assumed that the di erence between the emission 399.5nm and 399.61nm emissions fronts are su ciently similar for the purposes of the Kalman lter.

It is also interesting to note that the average value across the 55 SOLPS-ITER simulations as computed by the synthetic CIII and NII front locations are, respectively, 0.2156m and 0.1870m. This is somewhat in line with what has been reported by Jesse Koenders in [13] where there was a 2 3cm di erence between these two front locations.

(a) Scaled linear t of the y_{CIII} front location: f $_1$ n_N [10 ^{18}] + $_2$ p_0 1.

Term	Estimate	SE
(Intercept)	-0.015039	0.016018
$_1$	0.051372	0.0093215
$_2$	0.29517	0.021542
Model Statistics:		
Root Mean Squared Error: 0.0389		
R-squared: 0.817		

(b) Scaled linear t of the y_{NII} front location: f $_1$ n_N [10 ^{18}] + $_2$ p_0 1.

Term	Estimate	SE
(Intercept)	-0.051911	0.012247
$_1$	0.05098	0.0071272
$_2$	0.3082	0.016471
Model Statistics:		
Root Mean Squared Error: 0.0298		
R-squared: 0.891		

Figure 4.2: Two linearly regressed ts based on a synthetic diagnostic [14] of MANTIS in SOLPS-ITER which takes into account the emission from di erent ions in SOLPS-ITER from the ADAS database [1].

4.3 Target Quantity Fits

In this section the results of linearly regressing the state parameters to quantities associated with the conditions of the target are shown. Both linear and nonlinear polynomial ts are shown and their potential for predicting $q_?^{tar;max}$ will be explored in the proceeding sections. For SOLPS-ITER this is de ned as the maximum of each quantity (i.e., T_e, $q_?$, and $_{i;?}$) at the 96th column and across the 34 rows of cells. Where I have de ned the following physical quantities in SOLPS-ITER: T_e as te , $q_?$ as fhtx./sx , and $_{i;?}$ fnax./sx . The de nitions of these quantities can be found in the SOLPS-ITER manual [11]. The goodness of t is evaluated using the R-squared coe cient and the RMSE. There are plenty of other statistical tests for goodness of t, but these two parameters give a good understanding as to how far o the prediction might be from the SOLPS-ITER simulations. It is important to note that these coe cients and errors are based on normalized data.

Term	Estimate	SE
(Intercept)	12.76	0.70288
$_1$	-4.7549	0.63042
$_2$	-42.768	3.5993
$^2_2$	0.66199	0.2711
$_1$ $_2$	10.666	1.6651
$^2_2$	52.106	5.7432
$^2_1$ $_2$	-0.92434	0.38039
$_1$ $^2_2$	-5.7675	1.1711
$^3_2$	-20.957	2.9095
Model Statistics:		
Root Mean Squared Error: 0.214		
R-squared: 0.947		

(a) Scaled polynomial t of $q_{?}^{tar;max}$: f $1 + ^2_1 + _1 _2 + ^2_2 + ^2_1 : _2 + _1 : ^2_2 + ^3_2$. This transformation corresponds to (x) in 4.1.

Term	Estimate	SE
(Intercept)	115.1	9.6984
$_1$	-53.942	8.2028
$_2$	-633.08	69.331
$^2_2$	11.998	3.5344
$^2_1$	216.74	37.867
$_1$ $_2$	1278.9	174.98
$^2_2$	-37.995	11.661
$^2_1$ $_2$	-264.37	56.199
$_1$ $^2_2$	-1119.6	186.67
$^3_2$	27.737	8.8122
$^2_2$	98.75	27.635
$^2_1$ $^2_2$	360.08	71.57
$^3_1$ $^3_2$		
$^4_2$		
Model Statistics:		
Root Mean Squared Error: 0.946		
R-squared: 0.938		

(b) Polynomial t of $T_e^{tar;max}$: f $1 + ^2_1 + _1 _2 + ^2_2 + ^2_1 : _2 + _1 : ^2_2 + ^3_2 + ^2_1 : ^2_2 + _1 : ^3_2 + ^4_2$. This transformation corresponds to (x) in 4.1.

Term	Estimate	SE
(Intercept)	78.925	22.497
$_1$	-170.58	19.832
$_2$	826.9	70.986
$^2_2$	17.005	8.0851
$^2_1$	76.674	20.992
$_1$ $_2$	-538.23	53.349
$^2_2$		
Model Statistics:		
Root Mean Squared Error: 19.7		
R-squared: 0.925		

(c) Polynomial t of $^{tar;max}_{i;?}$: f $1 + ^2_1 + _1 _2 + ^2_2$. This transformation corresponds to ! (x) in 4.1.

Figure 4.3: The least-squares tted function relating the state parameters to critical target quantities over the 55 simulations. Here, Wilkinson notation is used [15] and therefore $_1$ and $_2$ correspond to coe cients multiplied by n_N, p_0 and respectively.

Term	Estimate	SE
(Intercept)	3.358	0.23245
$_1$	-0.52413	0.13527
$_2$	-2.2373	0.31262
Model Statistics:		
Root Mean Squared Error: 0.565		
R-squared: 0.578		

(a) Scaled linear t of $q_?^{tar;max}$: f $1 + _1 + _2$. This transformation corresponds to (x) in 4.1.

Term	Estimate	SE
(Intercept)	8.7818	1.0836
$_1$	-1.0771	0.63064
$_2$	-8.2677	1.4574
Model Statistics:		
Root Mean Squared Error: 2.63		
R-squared: 0.415		

(b) Linear t of $T_e^{tar;max}$: f $1 + _1 + _2$. This transformation corresponds to (x) in 4.1.

Term	Estimate	SE
(Intercept)	237.43	14.476
$_1$	-82.119	8.4242
$_2$	164.5	19.469
Model Statistics:		
Root Mean Squared Error: 35.2		
R-squared: 0.747		

(c) Polynomial t of $_{i;?}^{tar;max}$: f $1 + _1 + _2$. This transformation corresponds to (x) in 4.1.

Figure 4.4: The least-squares tted function relating the state parameters to critical target quantities over the 55 simulations. Here, Wilkinson notation is used [15] and therefore $_1$ and $_2$ correspond to coe cients multiplied by n_N , p_0 and respectively.

4.4 Kalman lter with Integration Model

These are the results of the Kalman lter applied with the Integration Model are applied to the two system identi cation and four control shots presented [13]. TheQ and R matrices were manually tuned using the shot which had a more aggressive reference to follow from [13] (i.e., #69145 and #69148). This gives greater con dence that the Kalman lter will be able to respond with more di cult request regarding the state of the divertor.

$$Q = \begin{matrix} 5 & 10^{6} \\ 0 & \end{matrix} \qquad \begin{matrix} 0 \\ 1 & 10^{6} \end{matrix} \qquad R = \begin{matrix} 0.01 & 0 \\ 0 & 0.01 \end{matrix}$$

These matrices are by no means optimal, but the Kalman filter does follow the measured signal well enough to be used in control applications. When tuning Q and R it was also taken into consideration how the state evolved and if that seemed intuitively realistic. For example, as the influx of gas makes its way into the tokamak it should be expected that the state parameters both increase to a certain extent. In some cases Q and R could be set to values which allow the output signal to be tracked with small residuals, but n_N would be stuck at zero which shouldn't hold physically given there is an increasing N_2 influx.

4.4.1 Kalman filter: Input, Output, and State

Below are the input, output and state evolutions for the different experiments mentioned above. To reiterate, the Kalman filter works out what the state evolution is by updating its prediction using the model 4.2. In other words, it uses the measurements coming from MANTIS and uses the synthetic diagnostic mappings 4.2b 4.2a from SOLPS-ITER to reconstruct what the SOLPS-ITER parameters n_N and p_0 should be.

The "Model" line in the figure below refers to the model 4.2 without any updates from the MANTIS measurements. This is to demonstrate how well the hand-tuned model would do on its own. The "filtered" line is the evolution of the the Kalman filter which has been updated on equations.

As stated in the methods section, to gain confidence that the Kalman filter is operating close to optimally, there are statistical indicator which can be checked. This is the mean of the residual. This test should indicate that the difference between the filtered signal is mostly white noise. In other words this means that Kalman filter has successfully reconstructed the state parameters to the degree that mostly only a random signal remains. There are other statistical tools to conclude that the signal truly is white noise and has the proper theoretical covariance [16], but a minimal mean was all that was used to tune the Q and R matrices in this thesis. This simple analysis is like what was employed in [7] to evaluate performance.

Also, given that the model has inherent imperfections and the assumptions about the noise and disturbances may be incorrect, the Kalman filter residual will never exhibit such optimal behavior. The analysis of the residuals as white noise should therefore be considered a theoretical benchmark of optimality for the Kalman filter that will not be met in practice. Luckily the residuals could be tuned such that the mean of the residuals is small relative to the scale of the distance of the 50% extinction fronts.

It is also important to note that the simulations were done from the very start of the MANTIS measurements, but the beginnings and endings were clipped because they contain transient information before the plasma starts up and after it ramps down. This transient information makes it difficult to say anything meaningful about the performance of the KF as the mean over the course of the entire shot is considerably affected.

Figure 4.5: From top to bottom: the input, state, output and KF residual evolutions from shot #69148. In the state and output plots, both show the model acting on its own without measurement updates.

The KF does a relatively good job at tracking the outputs signals while showing increasing

neutral pressure and nitrogen density. The reconstructed state was tuned to follow the modeled n_N more than p_0 as the former's evolution is based on clearer and simpler assumptions about an integration of the injected N_2. Consequently it should be observed that the evolution of p_0 takes up more of the form of the output evolution than n_N. Again, because n_N and p_0 exist only within the static simulation of SOLPS-ITER it is not currently possible to directly verify if this evolution is physical. With that being said, as the front position moves up, the area over which p_0 is averaged 3.2 would get cooler, potentially causing more recombination, and therefore increasing the neutral pressure.

The residuals exhibit very small means. In the case of the CIII front, the mean is exceptionally low on the order of 10^{-5}. Also, in both signals the transient jumps around 1.2 signals barely cause the residuals to deviate from 0 at all. This gives con dence in the robustness of the KF to track MANTIS signals.

Figure 4.6: Input, state, KF and output evolution during shot #69148.

Figure 4.7: From top to bottom: the input, state, output and KF residual evolutions from shot #69145. In the state and output plots, both show the model acting on its own without measurement updates.

Similar behavior is seen here where p_0 takes up more of the form of the output due to the tuning of Q and R. From [30] the neutral pressure, as measured by the baratron in the private flux region of TCV, is on the order of 0.1 Pa which gives some more confidence that this at least describes the right operating space. However, the baratron should not be seen as a proxy for p_0. First, [30] shows there is a model descrepancy between the synthetic baratron diagnostic and the real one. Second p_0 is simply not measurable by the baratron in the flux region, it is a quantity from SOLPS-ITER. One could make the argument that they are functionally related, but any conjecture as to how they are related should be studied in detail.

The residuals have relatively small means when compared to the scale the front locations operate on: around the order of mm's as opposed to tens of centimeters. This indicates a strong correlation and gives confidence in the operation of the KF. However, during the transient jump in the MANTIS signal close to 1.2 seconds, the residual exhibits a jump away from zero mean, meaning that the KF has trouble tracking transient effects. The KF performance is therefore seen to be worse for shot #69148 than for #69145. This might be because D_2 is what is actuating the front locations as opposed to N_2. Because the tuning is biased to track the evolution of the modeled n_N which is only dependent on the injection of N_2, that means that p_0 sees a more aggressive actuation by the KF to compensate for the rapid increase in the MANTIS signal. However, just actuating p_0 is not enough to catch up with the real signal during the transience.

4.4.2 Validation of KF Performance

An analysis of how the Kalman lter's reconstructed state parameters perform at predicting target parameters will be shown. This is important because the broader purpose of the Kalman lter is to be used with a controller which will make predictions on the conditions of the outer target several time samples ahead of the current time sample. The max perpendicular heat ux on the outer divertor target as predicted by the Kalman lter will be compared to a measurement of the same quantity by the vertical infrared camera (VIR) on the TCV. Note that the maximum heat ux by the VIR is de ned o ine a posteriori. That is, the position along the outer divertor is chosen which eventually experiences the highest perpendicular heat ux at some point in each experiment as measured by the VIR. This means slightly di erent locations of the outer target are compared from experiment to experiment and these also may not align with the location of $q_{\perp}^{tar;max}$ from the SOLPS-ITER simulations. However, the focus was on comparing $q_{\perp}^{tar;max}$ and not necessarily the location of it.

There are both linear and non-linear transformations to get to the max perpendicular heat ux on the outer divertor target in the analysis section. This is to show the reader that for a future controller it may be su cient to relate the model to the condition of the target via linear transformations only, possibly meaning a linear controller could be used which usually have better properties, especially for making guarantees about convergence.

Also note that some of the theoretical arguments given here also serve as a basis to explain the following validation section when the KF is combined with Koenders' Trasnformed Model.

Variables	De nitions
x	Linear transformation on x for $T_e^{tar;max}$ 4.4b
(x)	Non-linear transformation on x for $T_e^{tar;max}$ 4.3b
x	Linear transformation on x for $_{i;\perp}^{tar;max}$ 4.4c
$!(x)$	Non-linear transformation on x for $_{i;\perp}^{tar;max}$ 4:3c
$VIR_{q_{\perp}^{tar;max}}$	The $q_{\perp}^{tar;max}$ as measured by the VIR
(x)	Non-linear transformation on x for $q_{\perp}^{tar;max}$ 4.3a
x	Linear transformation on x for $q_{\perp}^{tar;max}$ 4.4a
$f(!(x); (x))$	Non-linear transformation on non-linearly derived $_{i;\perp}^{tar;max}$ and $T_e^{tar;max}$
$f(x; x)$	Non-linear transformation on linearly derived $_{i;\perp}^{tar;max}$ and $T_e^{tar;max}$

Table 4.1: Key for target analysis plots. Here $f()$ is the analytic function that was presented in 3.24. RMSE(a,b) means the root mean square error between a and b.

RMSE Variables	RMSE Values
RMSE(x, (x))	1.58
RMSE(x, ! (x))	2.92e+21
RMSE(VIR$_{q_\perp^{tar;max}}$, (x))	22557
RMSE(VIR$_{q_\perp^{tar;max}}$, (x))	44274
RMSE(VIR$_{q_\perp^{tar;max}}$, f (! (x); (x)))	43483
RMSE(VIR$_{q_\perp^{tar;max}}$, f (x; x))	41951

Table 4.2: RMSE values for differently regressed variables predicting $q_\perp^{tar;max}$. See 4.1 for a reference to what these variables mean.

$q_\perp^{tar;max}$ as measured by the VIR shows a decrease around 1.2 seconds, which is around where the step increase in the emission fronts were made. Similarly, $_{i;\perp}^{tar;max}$ and $T_e^{tar;max}$ also both show a decrease. This is likely because of the injection of N_2 to actuate the step response reducing. Due to recombination and ion-neutral collisions, it would make sense for the temperature and ion flux to decrease as energy in the plasma is radiated away and therefore number of ions decrease as neutrals increase [24]. Then, after the step down in emission front occurs, closer to the target, a similar increase in all three quantities occurs. All predictions besides (x) show this down-up trend. This is likely due to an artifact in the 2-D polynomial fit where (x) exhibits a local increase. It should be noted that (x) still exhibits the lowest RMSE for predicting the $q_\perp^{tar;max}$ as measured by the VIR. Also note that f (! (x); (x)) and f (x; x) both appear as underestimations relative to (x) and (x) because the analytic formula used for the former two predictions 3.24 only accounts for the perpendicular heat flux from the plasma.

At around 1.5 seconds, the N_2 influx stops which likely increases the electron temperature at the target and the ionization in divertor of the TCV. This would explain the reason that $q_\perp^{tar;max}$ sees an increase. It is interesting to note that (x) sees the least dynamic change and also has the lowest RMSE. This is likely due to (x) having a relatively small gradient around the center of the 55 simulation points.

RMSE Variables	RMSE Values
RMSE(x, (x))	1.67
RMSE(x, ! (x))	1.93e+21
RMSE(V IR$_{q_?^{tar;max}}$, (x))	47842
RMSE(V IR$_{q_?^{tar;max}}$, (x))	69679
RMSE(V IR$_{q_?^{tar;max}}$, f (! (x); (x)))	35909
RMSE(V IR$_{q_?^{tar;max}}$, f (x; x))	38553

Table 4.3: RMSE values for di erently regressed variables predicting$q_?^{tar;max}$. See 4.1 for a reference to what these variables mean.

Here, a steep decrease in the predictions is seen on$q_?^{tar;max}$ when D_2 is used to actuate the emission fronts, as opposed to the measured VIR$q_?^{tar;max}$ showing an increase. The electron temperature and ion ux both change according to the arguments in [24] with regards to D_2 fueling. In experiment #69148 a large injection of D_2 is seen at about 1.15 seconds. This leads to an initial increase in ionization which leads to a decrease in temperature. This increase in ionization should lead to an increase in the ionisation source which is seen as an increase in the ion ux at the target. In [24] the argument is also made that a decrease in the electron temperature directly necessitates an increase in the ion ux at the target. Forf (! (x); (x)) and f (x; x) it is shown that the decrease in$T_e^{tar;max}$ acts more strongly on$q_?^{tar;max}$ than the increase in $_{i;?}^{tar;max}$ between 1.1 and 1.2 seconds. After this, an increase in(! (x); (x)) and f (x; x) are seen as $_{i;?}^{tar;max}$ dominates over the now, much smaller,$T_e^{tar;max}$. This indicates a power limited regime [24] where the power for ionization is limited by the power entering the divertor.

(x), (x) exhibit similar behavior although slightly positively o set perhaps due to power from neutrals and so it becomes more di cult to theoretically justify the measured response from the VIR. Unidenti able power discrepancies between SOLPS-ITER and the VIR on the TCV have been seen before [30] where the VIR makes over estimations. Because the discrepancy happens when D_2 is injected it could fall under the candidate explanation, from [30], of the VIR being sensitive to emissions from the Pfund (n! 4) or Brackett (n ! 4) series of hydrogen. However, after this point of D_2 injection, the predictions begin to line up again with the VIR.

When the D_2 in ux is nally turned o around 1.55 seconds, the VIR measurement declines in magnitude. (x) dips slightly but doesn't follow the rate of change of the VIR measurement as well as f (! (x); (x)). This appears to be because(x) predicts a decline in the electron temperature

at the target. The behavior of f (! (x); (x)) seems to have more theoretical backing from [24] in the following way. First, ! (x) sees an initial increase when D_2 is shut o due to the ionization rate decreasing which necessitates an increase in the electron temperature at the target. However, because N_2 is continuing to be injected and radiating away power, this should mean a decrease in electron temperature at some point which is seen by (x) starting at around 1.6 seconds. (x) likely doesn't follow this trajectory because p_0 and/or n_N do not show a fast enough decrease. This could simply be an artifact of the linearly regressed t. As an alternative to these theoretical explanations as to why a decrease occurs when the D_2 valve is switched o is that the VIR measurement could simply be measuring less and less hydrogen radiation.

4.5 Koenders' Transformed Model

As stated in the methods section, the 55 SOLPS-ITER simulations were used in a scheme to linearly transform the output parameters of Koenders' model [13] y_{NII} and $\hat{n}_e$ into the state parameters of interest: n_N and p_0. There are therefore two R-squared values associated with this transformation: one between Koenders' output parameters and n_N and one between Koenders' output parameters and p_0.

Transformation	R-squared Value
$(y_{NII}, \hat{n}_e) \rightarrow n_N$	0.1435
$(y_{NII}, \hat{n}_e) \rightarrow p_0$	0.9386

Table 4.4: R-squared values for linearly transforming Koenders' di usion model to the desired SOLPS-ITER state parameters n_N and p_0.

It is apparent from the R-squared values that the linear transformation is more reliable for p_0 than for n_N. Along with the C and D matrices 4.2 which relate the SOLPS-ITER values of p_0 and n_N to y_{CIII} and y_{NII} the full state-space formulation becomes 3.15. The state matrices of the transformed model, $\tilde{A}$, $\tilde{B}$, and $\tilde{C}$ have dimensions of 80 80, 80 2 and 2 80 respectively and are thus too big to justify presenting here.

Although the system is Schur stable it is not observable or controllable. More explicitly, the rank of the observability and controlability matrices were found to be 20 and 62 respectively. This means that a unique evolution back to any initial condition x_0 from a set of measurements y cannot be guaranteed. Additionally, not all states can be in uenced by the input. However, because the system has no unstable modes it still means that the system is stabilizable and detectable. This essentially means that for those states which cannot be controlled or observed over time, they will naturally decay.

4.6 KF with Koenders' Transformed Model

The shots to which the Kalman lter using Koenders' transformed model was applied to the same six shots in the previous sections. Tuning the Q and R matrices was done di erently than for the Kalman lter using the integration. This is because Q is 80 80 and contains the standard deviations of the noise associated with the 80 state parameters in x which are also unknown in their physical de nition. Therefore a functional approach was taken to compute the 80 values along the diagonal Q. For the same reason, the state is not constrained as it was with the Integration Model.

This involved computing the eigenvalues of 3.15 and computing the inverse square of the real parts.

$$\mathrm{tr}(\tilde{Q}) = < (\mathrm{eig}(\tilde{A}))^{-2} \tag{4.4}$$

This ensures that those states which decay faster (i.e., have a relatively smaller real part to their eigenvalue) are subject to more uncertainty than those which decay more slowly. This can be demonstrated by making the following system:

$$\begin{aligned} \tilde{x}_{k+1} &= \tilde{A}\tilde{x}_k + \tilde{B}\tilde{u}_k \\ y_k &= I_{80\ 80}\tilde{x}_k \end{aligned} \tag{4.5}$$

In this way, a step response can be used to investigate y_k which is identical to $\tilde{x}_k$. A plot can then be made where each of the 80 state parameter step responses are colored by the real part of their eigenvalues 4.8. Because the $\tilde{A}$ matrix is sparse, only the first 40 states are actuated by N_2 and the last 40 states are actuated by D_2 so the plots are separated for clarity. Notice how the larger the real part, the longer the signal takes to decay to 0. The Q tuning above reflects trusting the darker red state parameters more than the dark blue ones.

Figure 4.8: Step response for the 80 $\tilde{x}$ parameters. Because the $\tilde{A}$ matrix is sparse, only the first 40 states are actuated by N_2 and the last 40 states are actuated by D_2. The dark blue signals are barely visible because they decay so quickly.

Once Q was established in this way, R was tuned manually from there based on minimizing the mean of the residual as before. This results in the following R matrix where the uncertainties in the measured output are set equal because they both come from MANTIS:

$$R = \begin{matrix} 1 & 10^{13} \\ 0 & 1 \end{matrix} \quad \begin{matrix} 0 \\ 10^{13} \end{matrix} \tag{4.6}$$

4.6.1 Kalman filter: Input, Output, and State

With this poorly transformed model, the KF is still able to capture enough of the dynamics to reasonably reconstruct the n_N and p_0. However, notice that because, in this model, n_N and p_0, do not belong to the state but to the transformation $C\tilde{x}$, they are therefore dependent on the same dynamically changing parameters and therefore appear to have almost identical, but proportionally different behavior. It is likely not physical that these parameters exhibit the same dynamics and so this is an inherent draw back to this approach. It should still be analyzed however how well n_N and p_0 can predict the heat flux in this case as the mean of the residual is relatively small for both fronts despite a positive bias.

Figure 4.9: From top to bottom: the input, state, output and KF residual evolutions from shot #69145. In the state and output plots, both show the model acting on its own without measurement updates.

Figure 4.10: From top to bottom: the input, state, output and KF residual evolutions from shot #69148. In the state and output plots, both show the model acting on its own without measurement updates.

Again, the states move in an identical fashion. It is unlikely that this is physical, but it does capture the dynamics measured by MANTIS. It is clear that this KF in either shot #69145 or #69148 follows the higher frequency dynamics more which consequently allows it to capture the step response better than the KF with the Integration Model. This can be seen because the residual barely moves from being centered around the zero-line through the shots.

4.6.2 Validation of KF Performance

The following are the results of a comparison between Koenders' transformed model with a KF to measurements from the VIR. This the same comparison as was made for the Integration Model so the same reference table 4.1 should be used to interpret the plots.

RMSE Variables	RMSE Values
RMSE(x, (x))	1.466
RMSE(x, ! (x))	5.12e+21
RMSE(VIR$_{q_?^{tar;max}}$, (x))	34922
RMSE(VIR$_{q_?^{tar;max}}$, (x))	42526
RMSE(VIR$_{q_?^{tar;max}}$, f (! (x); (x)))	88380
RMSE(VIR$_{q_?^{tar;max}}$, f (x; x))	84687

Table 4.5: RMSE values for differently regressed variables predicting $q_?^{tar;max}$. See 4.1 for a reference to what these variables mean.

The predictions f (! (x); (x)) and f (x; x) severely underestimate $q_?^{tar;max}$. Compared to the results from the Integration Model, the ion flux is about an order of magnitude lower. This could be due to the KF estimation of n_N reaching about double the max that the Integration Model does. Despite this possible explanation for the n_N dependent decrease in predicted $_{i;?}^{max;tar}$, it does not hold for the predictions of $q_?^{tar;max}$ based on n_N and p_0. That is, (x) and (x) follow the VIR signal quite well. This is likely due to the simple explanation that the fits for $_{i;?}^{max;tar}$ (i.e., ! (x) x 4.3 4.4) are much more negatively weighted for n_N than the fits for $q_?^{tar;max}$: (x) and (x).

RMSE Variables	RMSE Values
RMSE(x, (x))	2.90
RMSE(x, ! (x))	6.45e+21
RMSE(V IR$_{q_?^{tar;max}}$, (x))	78602
RMSE(V IR$_{q_?^{tar;max}}$, (x))	64308
RMSE(V IR$_{q_?^{tar;max}}$, f (! (x); (x)))	68496
RMSE(V IR$_{q_?^{tar;max}}$, f (x; x))	67087

Table 4.6: RMSE values for di erently regressed variables predicting$q_?^{tar;max}$. See 4.1 for a reference to what these variables mean.

As with the Integration Model there is a discrepancy in dynamics at around 1.15 seconds, where the predictions on$q_?^{tar;max}$ decrease while the measurement from the VIR increase. As with the Integration Model, (x) increases and levels out faster than the other predictions into what is assumed to be the power limited regime. However none of the predictions follow the decline which occurs in the VIR at 1.55 seconds. An inspection of the electron temperature and ion ux predictions does not match the theoretical argument given in [24] and reproduced by the Integration Model 4.3. That being said, (x) and (x) do follow the VIR signal in what is assumed to be the power limited regime well. Additionally, in this shot, the consequences of having the higher frequencies within the ltered n_N and p_0 is particularly apparent, especially around 0.7 seconds.

Chapter 5

Conclusions

The aim of this thesis is to demonstrate the use of a dynamic model, containing information from SOLPS-ITER, in combination with a Kalman filter, to reconstruct quantities belonging to SOLPS-ITER with the purpose of predicting divertor target conditions in real time. This research shows that given a sufficient number of static SOLPS-ITER simulations are done to cover a control-relevant operational space of a tokamak, then a dynamic model can be derived from these simulations completely offline which work sufficiently well in a control context when used with a KF. The broader implication of this is that studies can potentially be done completely off-line to design a control-relevant model which is also able to make predictions on the target condition. This is essential in the context of a fusion power plant where time and resources will be limited to iteratively tune a controller over several shots, and knowing the condition of and controlling the target conditions means reaching greater fusion power regimes.

5.1 Discussion

Two linear models were explored in combination with KFs and their predictions for the maximum perpendicular heat flux on the outer divertor target of the TCV were compared with real measurements taken by the VIR on the TCV across 6 L-mode experiments.

5.1.1 Methods

The methods can be conveniently split up into the following groups for discussion.

Sensors and Synthetic Diagnostics

The only sensor that is chosen for the KF presented in this thesis is MANTIS. If MANTIS fails for some technical reason, then there is no insight into what is happening in the divertor. Additionally, because the CIII and NII front locations are so similar, it is not as easy to argue that these parameters can uniquely identify a SOLPS-ITER simulation or some physical solution between simulations out of the 55, every time a measurement is taken. This uniqueness is needed to make the correct predictions on the divertor target, with respect to SOLPS-ITER.

It should also be noted that there are current discrepancies between SOLPS-ITER and real measurements taken on the TCV [30] which are currently being worked out by researchers at EPFL. This sets an undefined upperbound on how any model based on SOLPS-ITER can perform with this method. In other words, even if a unique simulation could be identified from real measurements on the TCV, it does not guarantee that the other quantities (like those describing the target condition) from those SOLPS-ITER simulations agree with reality.

The fits on the synthetic diagnostics are chosen to be linear, however the goodness of the fits should perhaps be called into question as they only have an R-squared value of around 0.8. Despite this the linear fits perform well in practice when applied to real signals in combination with a KF.

Dynamic Models

The Integration Model is extremely simple and works surprisingly well. The nature of its small dimensionality i.e., a 2 2 state means that it can be processed much faster than Koenders' Transformed Model, which is paramount for the use case of a predictive controller where prediction horizons scale strongly with dimensionality. There could have been better tuning parameters for Koenders' Transformed Model, but they were not found. With that being said, the trajectories of $q_?^{max;tar}$, $T_e^{max;tar}$, and $_{i;?}^{max;tar}$ from the Integration Model seem to match theoretical arguments better than Koenders' Transformed Model.

5.1.2 Results

It is di cult to say which model is better for the purposes of control as neither have been used in an active control loop. In terms of making predictions on $q_?^{max;tar}$ however the Integration Model performs better over the six control-relevant L-mode shots analyzed, with a minimum RMSE, with respect to the VIR-measured $q_?^{max;tar}$, of 42,280 W and a standard deviation of 3,661 W. The table below summarizes the results across the 6 L-mode experiments using the Integration Model.

RMSE Variables	Mean RMSE Values	Std of RMSEs
RMSE(x, (x))	1.483	0.125
RMSE(x, ! (x))	2.303e+21	4.078e+20
RMSE(VIR$_{q_?^{tar;max}}$, (x))	46675	16145
RMSE(VIR$_{q_?^{tar;max}}$, (x))	61515	11209
RMSE(VIR$_{q_?^{tar;max}}$, f (! (x); (x)))	42658	7066
RMSE(VIR$_{q_?^{tar;max}}$, f (x; x))	42280	3661

Table 5.1: Mean RMSE values and standard deviations of the RMSEs for each variable across six experiments when using the Integration Model

The same can also be seen over the six experiments when using Koenders' Transformed Model.

RMSE Variables	Mean RMSE Values	Std of RMSEs
RMSE(x, (x))	2.50	0.838
RMSE(x, ! (x))	5.887e+21	7.010e+20
RMSE(VIR$_{q_?^{tar;max}}$, (x))	69438	21705
RMSE(VIR$_{q_?^{tar;max}}$, (x))	56375	8622
RMSE(VIR$_{q_?^{tar;max}}$, f (!x; x))	77526	13644
RMSE(VIR$_{q_?^{tar;max}}$, f (x; x))	73653	11474

Table 5.2: Mean RMSE values and standard deviations of the RMSEs for each variable across six experiments when using the Koenders' Transformed Model

These tables should not be the nal indicator of performance. The chapter describing the results 4 goes into why some discrepancies between the measured $q_?^{tar;max}$ by the VIR may have di ered from the predictions and how the predictions tie in with current theoretical arguments about the divertor region of the TCV [24]. With that being said, the Integration Model with the KF does appear to agree with theory more than Koenders' Transformed Model with the KF does. Again, this behavior from Koenders' Transformed Model could be due to the poor performance of the transformation 4.4 or the fact that the variables predicting $q_?^{tar;max}$ (i.e., n_N and p_0) are forced to be simple linear combinations of the ltered signal.

5.2 Outlook

Future research should investigate using more diagnostics which have high a high enough acquisition frequency and react to the injection of N_2 and D_2. The idea here is to more uniquely relate the real plasma in the TCV to SOLPS-ITER simulations. The more different diagnostics, the more confidence one can have that measured quantities don't also belong to another plasma scenario on the TCV.

Bolometers and FIR are good sensors to look at first, but they must first have studies done on how they relate to SOLPS-ITER. A similar synthetic diagnostic should be developed as the one which shows promise in [30], but for the new RADCAM system. A synthetic diagnostic which can measure line-integrated electron densities which pass through the core are rather difficult to realize as SOLPS-ITER does not simulate the core. Instead, vertical integration lines could be investigated which do not pass through the core but do pass through the SOL as simulated by SOLPS-ITER. It may be advantageous to average over spectral chords for either the FIR or the bolometers. The idea here is that SOLPS-ITER may agree more over a spatial average than an integration of a single chord.

A linear KF is used in this thesis as the mappings from n_N and p_0 to the CIII or the NII front locations are made to be linear. It could be argued that a better fit might be a polynomial fit as this would lead to a higher R-squared value, but generally increasing complexity in a fit function should only be pursued if there is some physical basis for it. Changing the fit function without any real physical justification could lead to artifacts in the mappings which worsen performance. Additionally, if the dynamic evolution of n_N and p_0 leads outside of the parameter space defined by the SOLPS-ITER simulations a higher order polynomial (or some other more complex fit function) could result in dramatic changes to the predicted output. If an explicit fit function is not needed perhaps prediction techniques could be employed such as Gaussian Process Regressions.

5.2.1 Dynamic Model Improvements

The Integration Model's A and B could certainly be better identified than simply hand-tuning them as is done in this thesis. The difficulty with this optimization problem is that it is constrained by the solutions of C and D, the steady-state conditions 4.3, and that the evolution of x should be positive. A method was derived for this problem but could not be evaluated due to the computational cost involved C. This solves the problem of identifying a state-space identification problem with fixed C and D and equality constraints relating elements of A to elements of B.

Koenders' Transformed Model could be made much better by not making the poor linear transformation at all to SOLPS-ITER parameters as it done in this thesis. In other words, if a SOLPS-ITER synthetic diagnostic existed for the central line-integrated electron density, then no transformation would be necessary. One could simply transform the NII front location and central FIR line-integrated electron density directly to SOLPS-ITER parameters. However, one would run into the same problem that these SOLPS-ITER parameters would evolve the same over time A.8 as they would be subject to the same sensor dynamics, in the case that linear transformations are used. If it is not possible to develop a synthetic FIR for SOLPS-ITER, one could also refit Koenders' MIMO diffusion model parameters in the same way that is originally done in [12], for, say, specific bolometer chord measurements and the NII front location. The bolometer chords could pass through a part of the divertor region which is simulated by SOLPS-ITER. This would still mean that the states x being reconstructed from measurements would not directly be the SOLPS-ITER parameters.

Bibliography

[1] ix, 29

[2] Fervo energy - next-generation geothermal projects, 2024. 1

[3] Quaise energy, 2024. 1

[4] Terra power, 2024. 1

[5] Thorizon, 2024. 1

[6] S. C. Bates and K. H. Burrell. Fast gas injection system for plasma physics experiments. Review of Scienti c Instruments, 55(6):934 939, 06 1984. 10

[7] T.C. Blanken, F. Felici, C. Galperti, N.M.T. Vu, M. Kong, O. Sauter, M.R. de Baar, The EUROfusion MST1 Team, and The TCV Team. Real-time plasma state monitoring and supervisory control on tcv. Nuclear Fusion, 59(2):026017, jan 2019. 5, 13, 32

[8] R. A. CAIRNS. Tokamaks 3rd edition by john wesson, oxford university press 2004, 749pp, hardback 0 19 850922£135. Journal of Plasma Physics, 71(3):377 377, 2005. xi, 1, 7, 10

[9] D. Eldon, E. Kolemen, D.A. Humphreys, A.W. Hyatt, A.E. Jarvinen, A.W. Leonard, A.G. McLean, A.L. Moser, T.W. Petrie, and M.L. Walker. Advances in radiated power control at diii-d. Nuclear Materials and Energy, 18:285 290, 2019. 4

[10] Je rey P. Freidberg. Plasma Physics and Fusion Energy. Cambridge University Press, 2007. 1

[11] ITER. SOLPS-ITER, 2024. 29

[12] J.T.W. Koenders, A. Perek, C. Galperti, B.P. Duval, O. Fevrier, C. Theiler, M. van Berkel, and the TCV Team. Systematic design of a multi-input multi-output controller by model-based decoupling: a demonstration on tcv using multi-species gas injection. Nuclear Fusion, 63(10):106007, aug 2023. 5, 12, 13, 15, 21, 22, 23, 27, 49

[13] J.T.W. Koenders, A. Perek, B. Kool, O. Fevrier, T. Ravensbergen, C. Galperti, B.P. Duval, C. Theiler, M. van Berkel, The TCV Team, and The EUROfusion MST1 Team. Model-based impurity emission front control using deuterium fueling and nitrogen seeding in tcv. Nuclear Fusion, 63(2):026006, dec 2022. 9, 10, 12, 16, 20, 23, 27, 29, 31, 40, 72

[14] J.T.W. Koenders, M. Wensing, T. Ravensbergen, O. Fevrier, A. Perek, M. van Berkel, the TCV Team, and the EUROfusion MST1 Team. Systematic extraction of a control-oriented model from perturbative experiments and solps-iter for emission front control in tcv. Nuclear Fusion, 62(6):066025, apr 2022. ix, 9, 10, 12, 20, 28, 29

[15] MathWorks. Wilkinson Notation for Specifying Models, 2023. Accessed: 2024-09-12. ix, x, 30, 31

[16] Raman K. Mehra. Approaches to adaptive filtering. IEEE Transactions on Automatic Control, 17(5):693 698, 1972. 32

[17] Matthew Moynihan and Alfred B. Bortz. Tokamaks and Spherical Tokamaks, pages 123 151. Springer International Publishing, Cham, 2023. ix, 4

[18] R.A. Pitts, X. Bonnin, F. Escourbiac, H. Frerichs, J.P. Gunn, T. Hirai, A.S. Kukushkin, E. Kaveeva, M.A. Miller, D. Moulton, V. Rozhansky, I. Senichenkov, E. Sytova, O. Schmitz, P.C. Stangeby, G. De Temmerman, I. Veselova, and S. Wiesen. Physics basis for the first iter tungsten divertor. Nuclear Materials and Energy, 20:100696, 2019. iii, 3

[19] T. Ravensbergen, M. van Berkel, A. Perek, C. Galperti, B. P. Duval, O. Fevrier, R. J. R. van Kampen, F. Felici, J. T. Lammers, C. Theiler, J. Schoukens, B. Linehan, M. Komm, S. Henderson, D. Brida, and M. R. de Baar. Real-time feedback control of the impurity emission front in tokamak divertor plasmas. Nature Communications, 12(1):1105, 2021. 12

[20] T. Ravensbergen, M. van Berkel, S.A. Silburn, J.R. Harrison, A. Perek, K. Verhaegh, W.A.J. Vijvers, C. Theiler, A. Kirk, M.R. de Baar, and the EUROfusion MST1 team. Development of a real-time algorithm for detection of the divertor detachment radiation front using multi-spectral imaging. Nuclear Fusion, 60(6):066017, may 2020. 10

[21] Hannah Ritchie and Pablo Rosado. Energy mix. Our World in Data, 2020. 1

[22] U. A. Sheikh, L. Simons, B. P. Duval, O. Fevrier, D. Moret, A. Allegrucci, M. Bernert, F. Crisinel, T. Tersztyanszky, and O. Villinger. RADCAM A radiation camera system combining foil bolometers, AXUV diodes, and filtered soft x-ray diodes. Review of Scientific Instruments, 93(11):113513, 11 2022. ix, 11, 72

[23] Dan Simon. Optimal State Estimation: Kalman, H Infinity, and Nonlinear Approaches. Wiley-Interscience, USA, 2006. 7

[24] A Smolders, M Wensing, S Carli, H De Oliveira, W Dekeyser, B P Duval, O Fevrier, D Gahle, L Martinelli, H Reimerdes, C Theiler, K Verhaegh, and the TCV team. Comparison of high density and nitrogen seeded detachment using solps-iter simulations of the tokamak a configuration variable. Plasma Physics and Controlled Fusion, 62(12):125006, oct 2020. 9, 12, 15, 17, 38, 39, 40, 45, 48

[25] Andreas Smolders. Exploring observers and actuators for detachment control on the tcv tokamak. KU Leuven, 2019. xi, 10, 11, 12, 15, 16, 20, 25

[26] P C Stangeby. 60(4):044022, mar 2018. 25

[27] Peter C Stangeby. The plasma boundary of magnetic fusion devices. 2000. 3, 4, 25

[28] C. Theiler, B. Lipschultz, J. Harrison, B. Labit, H. Reimerdes, C. Tsui, W.A.J. Vijvers, J. A. Boedo, B.P. Duval, S. Elmore, P. Innocente, U. Kruezi, T. Lunt, R. Maurizio, F. Nespoli, U. Sheikh, A.J. Thornton, S.H.M. van Limpt, K. Verhaegh, N. Vianello, the TCV team, and the EUROfusion MST1 team. 57(7):072008, mar 2017. 25

[29] K. Verhaegh, B. Lipschultz, B.P. Duval, O. Fevrier, A. Fil, C. Theiler, M. Wensing, C. Bowman, D.S. Gahle, J.R. Harrison, B. Labit, C. Marini, R. Maurizio, H. de Oliveira, H. Reimerdes, U. Sheikh, C.K. Tsui, N. Vianello, W.A.J. Vijvers, the TCV team, and the EUROfusion MST1 team. An improved understanding of the roles of atomic processes and power balance in divertor target ion current loss during detachment. Nuclear Fusion, 59(12):126038, oct 2019. 10

[30] M. Wensing, H. Reimerdes, O. Février, C. Colandrea, L. Martinelli, K. Verhaegh, F. Bagnato, P. Blanchard, B. Vincent, A. Perek, S. Gorno, H. de Oliveira, C. Theiler, B. P. Duval, C. K. Tsui, M. Baquero-Ruiz, M. Wischmeier, TCV Team, and MST1 Team. SOLPS-ITER validation with TCV L-mode discharges. Physics of Plasmas, 28(8):082508, 08 2021. 11, 16, 22, 36, 39, 47, 49, 72

[31] Wykis. Deuterium-tritium fusion., 2007. ix, 2

Appendix A

Extra Shots

The rest of the experiments on which the models and KFs were tested.

A.1 Kalman Filter with Integration Model

Figure A.1: Comparison of plots and residuals for case 68861.

RMSE Variables	RMSE Values
RMSE(x, (x))	1.44
RMSE(x, ! (x))	2.00e21
RMSE(V IR $q_?^{tar;max}$, (x)))	53591
RMSE(V IR $q_?^{tar;max}$, x))	74161
RMSE(V IR $q_?^{tar;max}$, f (!x; x)))	31395
RMSE(V IR $q_?^{tar;max}$, f (x; x)))	37933

Table A.1: RMSE values for di erently regressed variables predicting $q_?^{tar;max}$

Figure A.2

RMSE Variables	RMSE Values
RMSE(x, (x))	1.53
RMSE(x, ! (x))	2.23+21
RMSE($VIR_{q_?^{tar;max}}$, (x))	28274
RMSE($VIR_{q_?^{tar;max}}$, (x))	48172
RMSE($VIR_{q_?^{tar;max}}$, f (!x; x))	44985
RMSE($VIR_{q_?^{tar;max}}$, f (x; x))	45393

Table A.2: RMSE values for di erently regressed variables predicting $q_?^{tar;max}$

Figure A.3

RMSE Variables	RMSE Values
RMSE(x, (x))	1.33
RMSE(x, ! (x))	1.94e+21
RMSE(V IR$_{q_?^{tar;max}}$, (x))	64760
RMSE(V IR$_{q_?^{tar;max}}$, (x))	64962
RMSE(V IR$_{q_?^{tar;max}}$, f (!x; x))	52398
RMSE(V IR$_{q_?^{tar;max}}$, f (x; x))	48377

Table A.3: RMSE values for di erently regressed variables predicting$q_?^{tar;max}$

Figure A.4

RMSE Variables	RMSE Values
RMSE(x, (x))	1.33
RMSE(x, ! (x))	2.80e+21
RMSE(V IR $q_?^{tar;max}$, (x))	63029
RMSE(V IR $q_?^{tar;max}$, (x))	67844
RMSE(V IR $q_?^{tar;max}$, f (!x; x))	47777
RMSE(V IR $q_?^{tar;max}$, f (x; x))	41471

Table A.4: RMSE values for di erently regressed variables predicting $q_?^{tar;max}$

A.2 KF with Koenders' Transformed Model

Figure A.5

RMSE Variables	RMSE Values
RMSE(x, (x))	2.398
RMSE(x, ! (x))	5.612e+21
RMSE(V IR$_{q_?^{tar;max}}$, (x))	77850
RMSE(V IR$_{q_?^{tar;max}}$, (x))	64743
RMSE(V IR$_{q_?^{tar;max}}$, f (!x; x))	51313
RMSE(V IR$_{q_?^{tar;max}}$, f (x; x))	52391

Table A.5: RMSE values for di erently regressed variables predicting$q_?^{tar;max}$